

# **Medium-Range Order in Amorphous Silicon Measured by Fluctuation Electron Microscopy**

**Final Report**

**23 June 1999–23 August 2002**

P.M. Voyles and J.R. Abelson  
*University of Illinois at Urbana-Champaign  
Urbana, Illinois*



**NREL**

**National Renewable Energy Laboratory**

1617 Cole Boulevard  
Golden, Colorado 80401-3393

NREL is a U.S. Department of Energy Laboratory  
Operated by Midwest Research Institute • Battelle • Bechtel

Contract No. DE-AC36-99-GO10337

# **Medium-Range Order in Amorphous Silicon Measured by Fluctuation Electron Microscopy**

## **Final Report**

**23 June 1999–23 August 2002**

P.M. Voyles and J.R. Abelson

*University of Illinois at Urbana-Champaign  
Urbana, Illinois*

NREL Technical Monitor: R. Matson

Prepared under Subcontract No. AAD-9-18668-04



# **NREL**

**National Renewable Energy Laboratory**

1617 Cole Boulevard  
Golden, Colorado 80401-3393

NREL is a U.S. Department of Energy Laboratory  
Operated by Midwest Research Institute • Battelle • Bechtel

Contract No. DE-AC36-99-GO10337

This publication was reproduced from the best available copy  
Submitted by the subcontractor and received no editorial review at NREL

### NOTICE

This report was prepared as an account of work sponsored by an agency of the United States government. Neither the United States government nor any agency thereof, nor any of their employees, makes any warranty, express or implied, or assumes any legal liability or responsibility for the accuracy, completeness, or usefulness of any information, apparatus, product, or process disclosed, or represents that its use would not infringe privately owned rights. Reference herein to any specific commercial product, process, or service by trade name, trademark, manufacturer, or otherwise does not necessarily constitute or imply its endorsement, recommendation, or favoring by the United States government or any agency thereof. The views and opinions of authors expressed herein do not necessarily state or reflect those of the United States government or any agency thereof.

Available electronically at <http://www.osti.gov/bridge>

Available for a processing fee to U.S. Department of Energy  
and its contractors, in paper, from:

U.S. Department of Energy  
Office of Scientific and Technical Information  
P.O. Box 62  
Oak Ridge, TN 37831-0062  
phone: 865.576.8401  
fax: 865.576.5728  
email: [reports@adonis.osti.gov](mailto:reports@adonis.osti.gov)

Available for sale to the public, in paper, from:

U.S. Department of Commerce  
National Technical Information Service  
5285 Port Royal Road  
Springfield, VA 22161  
phone: 800.553.6847  
fax: 703.605.6900  
email: [orders@ntis.fedworld.gov](mailto:orders@ntis.fedworld.gov)  
online ordering: <http://www.ntis.gov/ordering.htm>



Printed on paper containing at least 50% wastepaper, including 20% postconsumer waste

## Table of Contents

Abstract .....	1
1. Introduction .....	2
2. Fluctuation Electron Microscopy: Theory and Practice .....	3
3. Experimental Results on a-Ge and a-Si .....	8
3.1 Evaporate a-Ge and a-Si .....	8
3.2 Sputtered a-Si .....	8
3.3 Implant Amorphized a-Si .....	10
4. Structural Models .....	11
5. Experimental Result on a-Si:H and Discussion .....	17
5.1 Stability of Paracrystalline Grains .....	19
5.2 Photostructural Changes in a-Si:H .....	23
6. Conclusions and Future Prospects .....	24
6.1 Implications of the Paracrystalline Model .....	24
6.2 Depth dependence of MRO .....	24
6.3 Study of Amorphous Alloys .....	25
6.4 Variable Resolutions FEM Using Nanodiffraction .....	25
6.5 Other methods for characterizing MRO .....	26
Acknowledgements .....	27
Publications Resulting from NREL Support .....	27
References .....	28

## List of Figures

Figure 1: Diagram of the effective search volumes, indicated in gray, of $g_2(r)$ and $g_3(r_1, r, q)$ .....	2
Figure 2: A simplified ray diagram of a TEM in the hollow-cone dark-field mode used for FEM imaging .....	4
Figure 3: Typical $V(k)$ data for a-Si. The positions of diffraction peaks in crystalline and amorphous silicon are shown for reference .....	5
Figure 4: Qualitative picture of $V$ from two prototypical samples: (a) a completely random collection of atoms and (b) a sample consisting of randomly oriented ordered clusters .....	6
Figure 5: $V(k)$ for magnetron sputtered a-Si films as a function of substrate temperature during growth .....	9
Figure 6: $V(k)$ for magnetron sputtered a-Si films as a function of the flux ratio of low energy $Ar^+$ ions ( $J^+$ ) to depositing Si atoms ( $J^0$ ) at a constant substrate temperature of 230°C .....	10
Figure 7: $V(k)$ simulations for a several CRN models prepared using different energy minimization schemes, different system sizes, and different empirical potentials .....	11
Figure 8: $V(k)$ simulations for three early Keblinski paracrystalline structural models and the Stillinger-Weber CRN .....	12
Figure 9: $g_2(r)$ for the Keblinski model PC-K1 [26, 36] and a Nakhmanson PC model compared to experimental data for a-Si measured by x-ray diffraction .....	13
Figure 10: The $6_2 \cdot 6_2 \cdot 6_2 \cdot 6_2 \cdot 6_2 \cdot 6_2 \cdot 29$ Schläfli cluster of crystalline Si .....	15
Figure 11: The topologically crystalline grains in models PC-K1 and PC-K2 .....	16

Figure 12:	The simulated variable resolution correlation length $L$ as a function of the percent of atoms in the model involved in the paracrystalline grains.....	17
Figure 13:	$V(k)$ for a-Si:H films grown by plasma CVD (i) at USSC with large $H_2$ dilution of $SiH_4$ ('edge' material) and (ii) at the Ecole Polytechnique with a high pressure of $SiH_4$ (the 'polymorphous' regime) .....	18
Figure 14:	Dark field TEM images (for $k = 0.55 \text{ \AA}^{-1}$ ) and the unaveraged $V(k)$ traces for two different locations on the $H_2$ diluted USSC film.....	18
Figure 15:	Unaveraged $V(k)$ traces from different areas of samples of polymorphous a-Si:H deposited using higher (left) and lower (right) pressures of $SiH_4$ .....	20
Figure 16:	$V(k)$ for a-Si:H grown by magnetron sputtering using either $H_2$ or $D_2$ injected into the plasma; the use of $D_2$ <i>reduces</i> the variance $V(k)$ due to increased momentum transfer to paracrystalline grains, which relax towards a CRN .....	21
Figure 17:	$V(k)$ for the a-Si:H samples of Figure 12 in the as-deposited state, after light soaking (LS), and after light soaking plus thermal annealing (LS + AN) .....	22

# Medium-Range Order in Amorphous Silicon Measured by Fluctuation Electron Microscopy

Paul M. Voyles and John R. Abelson

Department of Materials Science and Engineering, and the  
Frederick Seitz Materials Research Laboratory,  
University of Illinois at Urbana-Champaign

## Abstract

Despite occasional experimental hints, medium range structural order in covalently bonded amorphous semiconductors had largely escaped detection until the advent of fluctuation electron microscopy (FEM) in 1996. Using FEM, we find that every sample of amorphous silicon and germanium we have investigated, regardless of deposition method or hydrogen content, is rich in medium range order. The paracrystalline structural model, which consists of small, topologically ordered grains in an amorphous matrix, is consistent with the FEM data; but due to strain effects, materials with a paracrystalline structure appear to be amorphous in diffraction measurements.

We present measurements on hydrogenated amorphous silicon deposited by different methods, some of which are reported to have greater stability against the Staebler-Wronski effect. FEM reveals that the matrix material of these samples is relatively similar, but the order changes in different ways upon both light soaking and thermal annealing. Some materials are inhomogeneous, with either nanocrystalline inclusions or large area-to-area variation in the medium range order. We cite recent calculations that electronic states in the conduction band tail are preferentially located around the boundaries of the nm-scale paracrystalline regions which we have identified. This is new evidence in support of spatially inhomogeneous conduction mechanisms in a-Si.

The key discovery in our work is that *all* samples of amorphous silicon must be described as having nm-scale topological crystalline order. This strongly modifies the long standing model of a covalent random network. Our new understanding of medium-range order must be considered in all future models of electronic properties and the Staebler-Wronski effect.

## 1. Introduction

Measuring medium-range structural order in glassy materials is a long-standing problem. Kinematic diffraction measurements reveal that glasses such as  $\text{SiO}_2$  share the same short-range bonding as their crystalline counterparts. Similarly, pure amorphous (a-Si) has approximately the same nearest-neighbor distance, mean coordination, and bond angle distribution as crystalline Si.

The difference between amorphous and crystal structures must therefore lie at distances outside the first coordination shell. Zachariasen proposed the continuous random network (CRN) model in 1932 as a structure with a uniform distribution of dihedral angles  $P(\phi)$  [1], but this proposal has been surprisingly hard to test. CRN models constructed by computer with an essentially random  $P(\phi)$  have reproduced the x-ray structure factor. In simulations of the electronic structure, these models also yield reasonable values for the band gap and band tails [2, 3]. However, all these characteristics depend mostly on nearest neighbor or next-nearest neighbor coordination and strain.

The underlying problem is that high energy kinematic scattering probes like x-ray or electron diffraction or EXAFS are related to the pair correlation function  $g_2(r)$  [4], which is proportional to the probability that two atoms in the sample are separated by a distance  $r$ . For a-Si, the best experimental measurement of  $g_2(r)$  [5, 6] shows a clear first-neighbor peak, centered on the crystalline nearest neighbor distance, but broadened somewhat by bond length and particularly by bond angle disorder. Second, third, and fourth neighbor peaks are also visible, but after that  $g_2(r)$  has no more structure. This is not a failure in the experiment, but a fundamental difficulty with  $g_2(r)$ . As shown in Figure 1,  $g_2(r)$  samples the structure in shells of inner radius  $r$  and outer radius  $r + dr$ , counting the number of atoms in each shell. For large  $r$ , even small bond angle distortions in the structure produce so many patterns of bonds that put an atom in the shell for any  $r$  that there is no significant structure in  $g_2(r)$ . It just increases smoothly as  $r^2$ , the surface area of the shell.

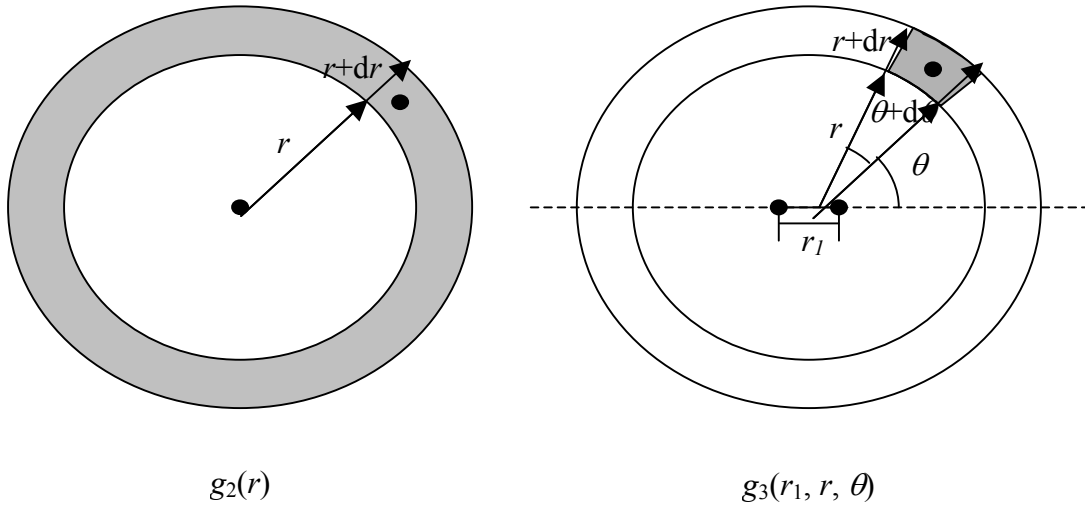


Figure 1: Diagram of the effective search volumes, indicated in gray, of  $g_2(r)$  and  $g_3(r_1, r, q)$ .  $g_2(r)$  searches a spherical shell between  $r$  and  $r+dr$ .  $g_3(r_1, r, q)$  searches a small portion of that shell between  $r$  and  $r+dr$  and  $q$  and  $q+dq$ .  $q$  is measured with respect to  $r_1$ .  $g_4(r_1, r_2, r, q)$  is even more selective: it searches a similar volume, but selects only a pair of atoms separated by a distance  $r_2$ .

There have been some tantalizing glimpses of subtle structure at longer range. Bellisent *et al.* [7] and Menelle [8] have reported small angle neutron scattering data for a-Si:H, which is mostly sensitive to the distribution of H, which is inconsistent with a uniform H distribution. Menelle interpreted the data in terms of a “filamentary” structure of H on a nanometer length scale, which suggests some structure in the underlying Si network. Small-angle x-ray scattering measurements also suggest some medium-range structure, which tends to be ascribed to “microvoids” [9]. Proton NMR [10], near-edge x-ray absorption fine structure [11, 12], and Raman spectroscopy measurements [13, 14] all suggest some form of structure, but have not been able to determine its character. These probes are sensitive to longer-range structure through multiple scattering of the probe (*i.e.* NEXAFS) or through probing the vibrational modes at low frequency and therefore longer range (Raman), but detailed structural information is very difficult to extract because of the complicated interaction of the probe with the sample atoms.

Structure at the nanometer length scale, which we will call medium-range order (MRO), is even challenging to define in a meaningful way. Zachairesen’s original proposal leads to one suggestion: MRO is a nonuniform distribution of dihedral angles, which involves fourth-neighbor atoms. Luedtke and Landman measure MRO by correlations between adjacent dihedral angles [15], and Elliot has suggested a hierarchy of terminology for different length scales [16]. We could also discard atomic position information entirely, and analyze the network in terms of its bonding topology. Ring statistics, which count the number of closed paths of bonds as a function of the number of bonds in the path, are one possible approach [17]. These measures can all be calculated for computer models, but we are not aware of any experimental probes which have been shown to correlate strongly with any of them.

Operationally, we define medium-range order as physical structure beyond the length scale which produces peaks in  $g_2(r)$ , but below the length scale which yields Bragg peaks in the structure factor. For a-Si, this experimentally unexplored territory extends from  $r = 8 \text{ \AA}$ , the diameter of the fourth coordination shell, to  $r = 30\text{-}50 \text{ \AA}$ , the minimum crystallite size which shows sharp Bragg peaks in x-ray diffraction.

We can access direct structural information from this entire range using fluctuation electron microscopy (FEM). In this paper we first describe FEM and summarize the experimental results on pure amorphous germanium (a-Ge), silicon (a-Si), and hydrogenated amorphous silicon (a-Si:H). We then describe the *paracrystalline* structural concept which we have developed to explain these results, and the computer models we have used to test this proposed structure. We also discuss the topological measurement of MRO using Schläfli cluster analysis, which is particularly well-suited to understanding paracrystalline structures. We then present detailed results on a-Si:H and discuss the differences created by various deposition methods and by post-deposition treatments. We conclude with a brief description of the future of FEM measurements and other possible characterizations of MRO using the electron microscope.

## 2. Fluctuation Electron Microscopy: Theory and Practice

In fluctuation electron microscopy, one utilizes the electron microscope at *nanometer-scale* (rather than atomic) spatial resolution to measure high-energy diffraction as a function of position across the sample. This provides a statistical measurement of MRO. The TEM typically uses an electron beam with an energy of 100-300 keV, so the majority of the interaction with the sample is kinematic scattering from the atom



cores. The scattering can be analyzed using the first Born approximation and the structural interpretability that comes with it.

Fluctuation electron microscopy is the study of the second moment, or variance  $V$ , of the diffracted intensity from nanometer-sized volumes. If  $I(\mathbf{r}, \mathbf{k}, Q)$  is a measure of the diffracted intensity from the sample as a function of position  $\mathbf{r}$ , diffraction vector  $\mathbf{k}$ , and spatial resolution proportional to  $1/Q$ , then

$$V(k, Q) = \frac{\langle I^2(\mathbf{r}, \mathbf{k}, Q) \rangle}{\langle I(\mathbf{r}, \mathbf{k}, Q) \rangle^2} - 1, \quad (1)$$

where  $\langle \rangle$  indicates averaging over position  $\mathbf{r}$ .

As originally proposed by Treacy and Gibson [18],  $I(\mathbf{r}, \mathbf{k}, Q)$  is measured by dark-field TEM. A simplified ray diagram of this imaging mode is shown in Figure 2.

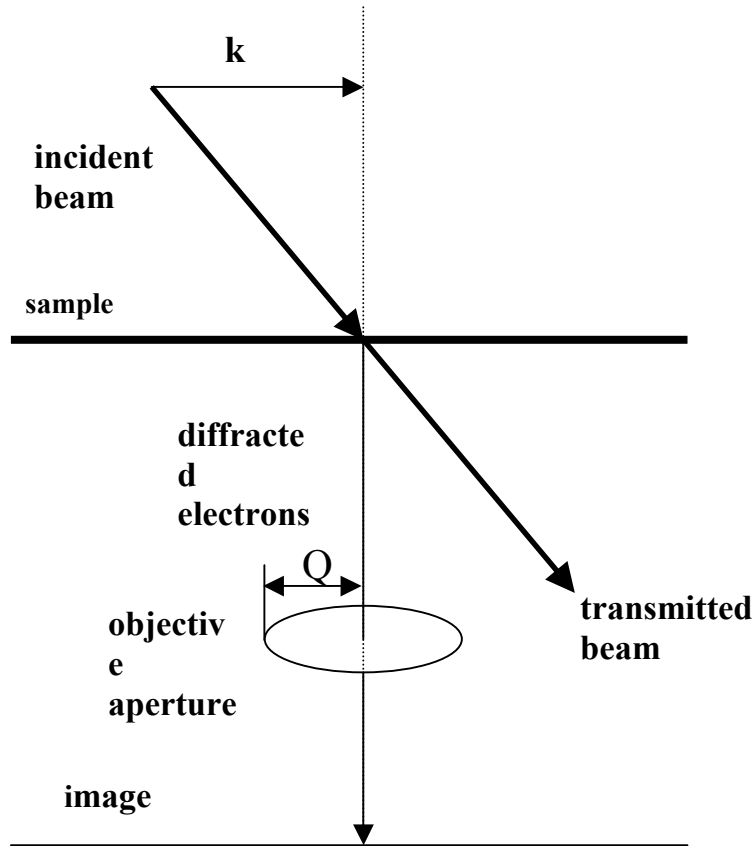


Figure 2: A simplified ray diagram of a TEM in the hollow-cone dark-field mode used for FEM imaging. All of the angles are greatly exaggerated; in a real TEM the beam stays within a few degrees of the optic axis.

The incident electron beam is tilted away from the optic axis of the microscope, and a small objective aperture is placed below the sample in the diffraction plane. This arrangement ensures that only electrons that have scattered through a diffraction vector  $\mathbf{k}$  pass through the aperture and continue on to form the image. The unscattered beam is blocked by the aperture, so areas of the images with no sample appear dark, therefore “dark-field” imaging. The aperture has a radius in diffraction space  $Q$ , so the real-space point spread function is approximately an Airy function of

width  $0.61/Q$ , which determines the spatial resolution. Since disordered materials tend to be isotropic, it is also useful to sweep the incident beam around in a circle with constant tilt angle to create an incident hollow cone of illumination. This averages over all the possible directions which have a constant scattering vector of magnitude  $k$ ; the resulting images look like the insets in Figure 3. This cone of illumination also facilitates the detection of larger nanoparticles embedded in the amorphous matrix, as shown in Section 5. The same data set can also be collected by nanodiffraction measurements, which we discuss in the last section. To obtain quantitative FEM data, one must make strictly linear measurements of image intensity, remove the effects of any large-scale non-uniformities in the sample, and properly treat sources of statistical noise in the data [19, 20]. Except as noted, the variance curve is the average of ten data sets taken on different areas of the sample, and the error bars represent one standard deviation from the mean, which is typically larger than errors from statistical noise.

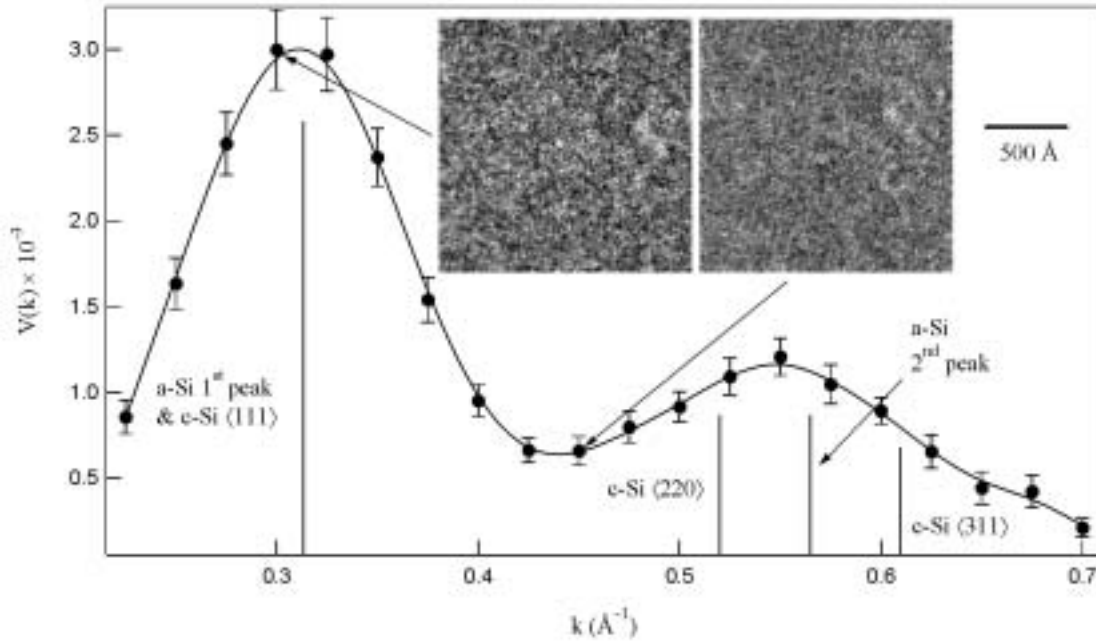


Figure 3: Typical  $V(k)$  data for a-Si. The positions of diffraction peaks in crystalline and amorphous silicon are shown for reference. Insets show dark field images with the characteristic ‘speckle’ pattern of amorphous materials at values of  $k$  corresponding to high and low image variance.

We can think of an image like those in Figure 3 as a map of the diffracted intensity from nanometer-scale volumes of the sample. For a qualitative understanding of how the variance of such a map is sensitive to MRO, consider  $V(k)$  from two different prototypical samples, as shown in Figure 4 [21]. The first sample, Figure 4(a), is a completely random distribution of atoms. If we cut out nanometer-sized volumes of this sample, each contains 20-30 atoms, which is enough to reflect the overall randomness of the sample, so they all have statistically similar structures. The diffracted intensity from each volume will be similar, and that yields a map with a low  $V$ . The second sample, Figure 4(b), consists of randomly oriented, nanometer-sized regions of correlated structure, i.e., crystals. Some volumes therefore contain a crystal oriented on a Bragg condition, which gives rise to a large diffracted intensity. Other volumes contain a crystal oriented between Bragg conditions, which gives rise to a very small diffracted intensity. That describes a map with a high variance.

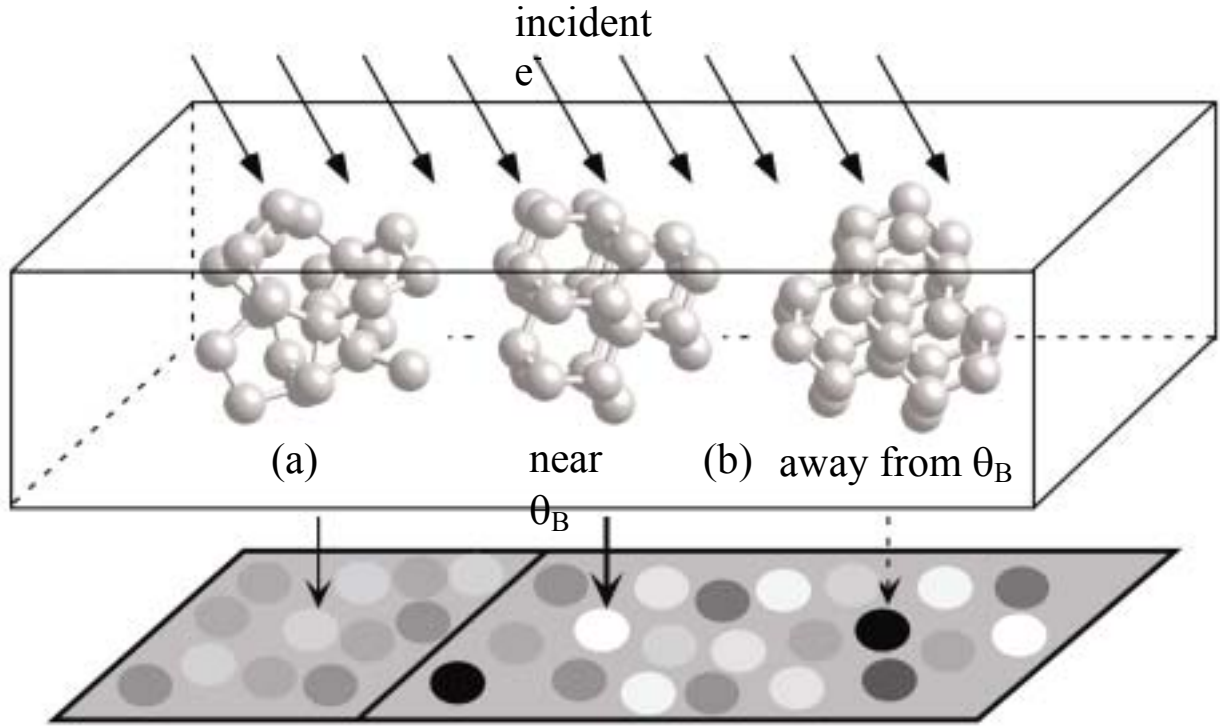


Figure 4: Qualitative picture of  $V$  from two prototypical samples: (a) a completely random collection of atoms and (b) a sample consisting of randomly oriented ordered clusters.  $V$  for sample (a) is small and shows little dependence on the imaging conditions.  $V$  for sample (b) is large, and varies significantly with the imaging conditions. Taken from Ref. [21].

What happens if we then change the imaging conditions? Changing  $k$  means changing the diffracting condition. For the random sample this will not matter, since there aren't any prominent pair spacings, and  $V(k)$  is essentially constant. For the ordered sample,  $V(k)$  will have maxima and minima at positions corresponding to maxima and minima in the structure factor of the crystals, as shown in Figure 3; beneath  $V(k)$  we also indicate the  $k$  values corresponding to typical diffraction peaks in crystalline and amorphous silicon. Changing  $Q$  at fixed  $k$  means changing the sampling volume (via the spatial resolution). For the random sample, as long as the sampling volume is large enough to contain "many" atoms, each volume reflects the average structure, and  $V(Q)$  is constant. For the ordered sample, when the sampling volume is small with respect to the size of the crystals, each region is sampled many times, giving the same intensity each time, which leads to a small  $V$ . When the sampling volume is comparable to the size of the crystals,  $V(Q)$  is at a maximum. For larger sampling volumes, more and more crystals become included within in each volume, the structure of the volumes approaches the average sample structure, and  $V(Q)$  decreases again.

This example shows qualitatively that a low  $V$  with little structure in  $k$  and  $Q$  indicates a sample with little or no MRO, while a large  $V$ , with significant structure in  $k$  and  $Q$  indicates a sample with significant MRO. Similar considerations dictate that a perfect crystal imaged with large enough resolution that individual atoms are invisible will have  $V = 0$ . As we discuss below, these broad statements are borne out by  $V(k, Q)$  simulations on various computer models.

Mathematically,  $\langle I(\mathbf{k}) \rangle$  for electrons, just like for x-rays, depends on only the two-body correlation function,  $g_2(r)$ , and is given by [22]

$$\langle I(\mathbf{k}, Q) \rangle = C_1(\mathbf{k}) \left( 1 + \rho \int_s g_2(\mathbf{r}) F_k(\mathbf{k}) a_Q(\mathbf{r}) d^3 \mathbf{r} \right). \quad (2)$$

$a_Q(\mathbf{r})$  is the point spread function of the microscope, given by the Airy function.  $F_k(\mathbf{k})$  describes the illumination conditions. For simple tilted illumination it is an exponential phase factor. For hollow-cone illumination, it is a  $J_0$  Bessel function.  $C_1(\mathbf{k})$  is a function describing scattering from a single atom, and contains no structural information. All the imaging equations are derived in detail and in consistent notation in Ref. [23].

$\langle I^2(\mathbf{k}) \rangle$ , however, depends on the three and four-body correlation functions as well<sup>1</sup> [22], and it is these objects which contain information about MRO [21]. Schematically,

$$\langle I^2(\mathbf{k}, Q) \rangle = C_2(\mathbf{k}) \left\{ \begin{aligned} & B_1 + B_2 \int_s g_2(\mathbf{r}) F_2(\mathbf{k}) a_2(\mathbf{r}) d^3 \mathbf{r} \\ & + B_3 \int_s g_3(\mathbf{r}_1, \mathbf{r}_2) F_3(\mathbf{k}) a_3(\mathbf{r}) d^3 \mathbf{r}_1 d^3 \mathbf{r}_2 \\ & + B_4 \int_s g_4(\mathbf{r}_1, \mathbf{r}_2, \mathbf{r}_3) F_4(\mathbf{k}) a_4(\mathbf{r}) d^3 \mathbf{r}_1 d^3 \mathbf{r}_2 d^3 \mathbf{r}_3 \end{aligned} \right\}. \quad (3)$$

$F_2(\mathbf{k})$ - $F_4(\mathbf{k})$  are combinations of multiple  $F_k(\mathbf{k})$  functions, and  $a_2(\mathbf{r})$ - $a_4(\mathbf{r})$  are combinations of multiple  $a_Q(\mathbf{r})$  functions.  $B_1$ - $B_4$  are constants, and  $C_2(\mathbf{k})$  describes the structure-independent scattering from single atoms. In an isotropic medium, the vector forms of  $g_3(\mathbf{r}_1, \mathbf{r}_2)$  and  $g_4(\mathbf{r}_1, \mathbf{r}_2, \mathbf{r}_3)$  reduce to  $g_3(r_1, r, \theta)$  and  $g_4(r_1, r_2, r, \theta)$ , respectively.  $g_3(r_1, r, \theta)$  and  $g_4(r_1, r_2, r, \theta)$  retain information at longer length scales than  $g_2(r)$ , because their sampling volume is smaller and more selective, as indicated schematically in Figure 1  $g_4(r_1, r_2, r, \theta)$  can be thought of as a pair-pair correlation function:  $r_1$  defines one pair separation,  $r_2$  defines another,  $r$  is the pair-pair separation, and  $\theta$  is the relative angle between the pairs. The  $g_4(r_1, r_2, r, \theta)$  sampling volume therefore has two atoms at the origin instead of one, and samples at a distance between  $r$  and  $r + dr$ , and at an angle between  $\theta$  and  $\theta + d\theta$ . Ref. [21] discusses these ideas in greater detail and provides some supporting model calculations.

There are two possible FEM techniques: *variable coherence* microscopy involves systematically varying  $k$  at constant  $Q$ . This is easily accomplished in the dark-field imaging mode shown in Figure 2 by changing the tilt angle of the incident beam, which can be done electronically. The height of the peaks in  $V(k)$  is related to the degree of MRO in the sample, and the positions are related to the internal structure of any ordered regions. All of the experimental results discussed here were acquired in this mode.

---

<sup>1</sup> In earlier work, Gibson and Treacy had incorrectly assumed that the three-body correlation term would integrate to zero, and that the four-body term would be the lowest-order function conveying MRO information. It was later realized that the three-body term must also be considered.

*Variable resolution* microscopy involves systematically varying  $Q$  at constant  $k$ . This is more difficult in dark-field imaging, since  $Q$  is controlled by the physical size of the aperture, which is only a few microns and would need to be changed mechanically. (A continuously variable mechanical aperture with the necessary capabilities has not, to our knowledge, been constructed.) Variable resolution FEM has been shown in simulations to give a quantitative measure of a characteristic MRO length scale of the sample. Preliminary measurements of this type have recently been demonstrated using a scanning TEM in nanodiffraction mode; variable resolution is achieved using a virtual objective aperture the effective size of which is controlled electronically [20].

Measuring the full data set  $V(k, Q)$  gives a *fluctuation map*, which contains the most possible information. A longer-term goal in FEM is to invert the data contained in the fluctuation map to extract  $g_3$  and  $g_4$ ; this is a major theoretical challenge. At present, we perform iterative simulations using model structures, discussed in Section 4 below, to calculate the variance  $V$  which is compared with experiment.

### 3. Experimental Results on a-Ge and a-Si

Much of the FEM work to date has examined unhydrogenated amorphous germanium (a-Ge) and silicon (a-Si) films because reliable structural models of these materials can be constructed in the computer [24] and used to simulate FEM data, which can be compared with experiment. It remains a considerable challenge to generate a reliable model which contains bonded H. The a-Ge and a-Si films exhibit structural differences as a function of substrate temperature during growth and upon post-growth thermal annealing; these and related observations provide strong evidence for the paracrystalline structural model, described in the next section.

**3.1 Evaporated a-Ge and a-Si:** Gibson and Treacy studied evaporated a-Ge films using FEM [25] and determined that (i) the variance  $V(k)$  exhibits peaks at  $k \sim 0.31$  and  $0.58 \text{ \AA}^{-1}$  (the latter of larger magnitude) which are inconsistent with a CRN structure, and can only be explained by the presence of significant MRO; and (ii) the variance peak intensities decrease by a factor of  $\sim 3$  upon annealing the film in situ at  $350^\circ\text{C}$  for 15 minutes. The reduction in  $V(k)$  implies that the films relax towards a structure with *less* MRO, i.e., a CRN. This is contrary to the assumption in the literature that annealing an amorphous film not only increases the short range order (as observed experimentally by others), but also the MRO. The authors concluded that the MRO in the as-deposited film was metastable with respect to a CRN structure. Treacy *et al.* found a similar effect in films of a-Si [26] but of smaller magnitude; the authors concluded that the as-evaporated a-Si films were more relaxed than those of a-Ge. It has since been found [27] that structural changes in a-Si films are strongly suppressed by the presence of a native oxide, which provides a second possible explanation for the smaller reduction in  $V(k)$  upon annealing.

**3.2 Sputtered a-Si:** We investigated the MRO in a-Si films deposited by magnetron sputtering of a Si target in an Ar plasma as a function of the substrate temperature [28, 29] or the  $\text{Ar}^+$  ion flux to the growth surface [30]. Both variables are expected to influence the dynamics of adatom incorporation, which provides a way to probe the formation mechanisms of MRO. The low pressure (1 mTorr) sputtering conditions yield films with mass density 98 % that of c-Si, and an unintentional H content of  $\sim 0.1$  at. %.

For substrate temperatures of  $200\text{--}350^\circ\text{C}$ , the electron structure factor  $S(k)$  remained nearly constant and indistinguishable from that of a CRN; at the next highest

temperature of 440°C, the c-Si  $\langle 220 \rangle$ ,  $\langle 311 \rangle$ , and higher order peaks were clearly observed, and nanocrystals  $\sim 150$  Å in diameter were seen in TEM images. By contrast, the  $V(k)$  peaks exhibited a *continuous* increase in amplitude over the temperature range of 200–300°C, as shown in Figure 5, and at 440°C  $V(k)$  became dominated by the presence of the nanocrystals. Thus, the MRO increased monotonically up to a growth condition at which nanocrystals were detected by diffraction.

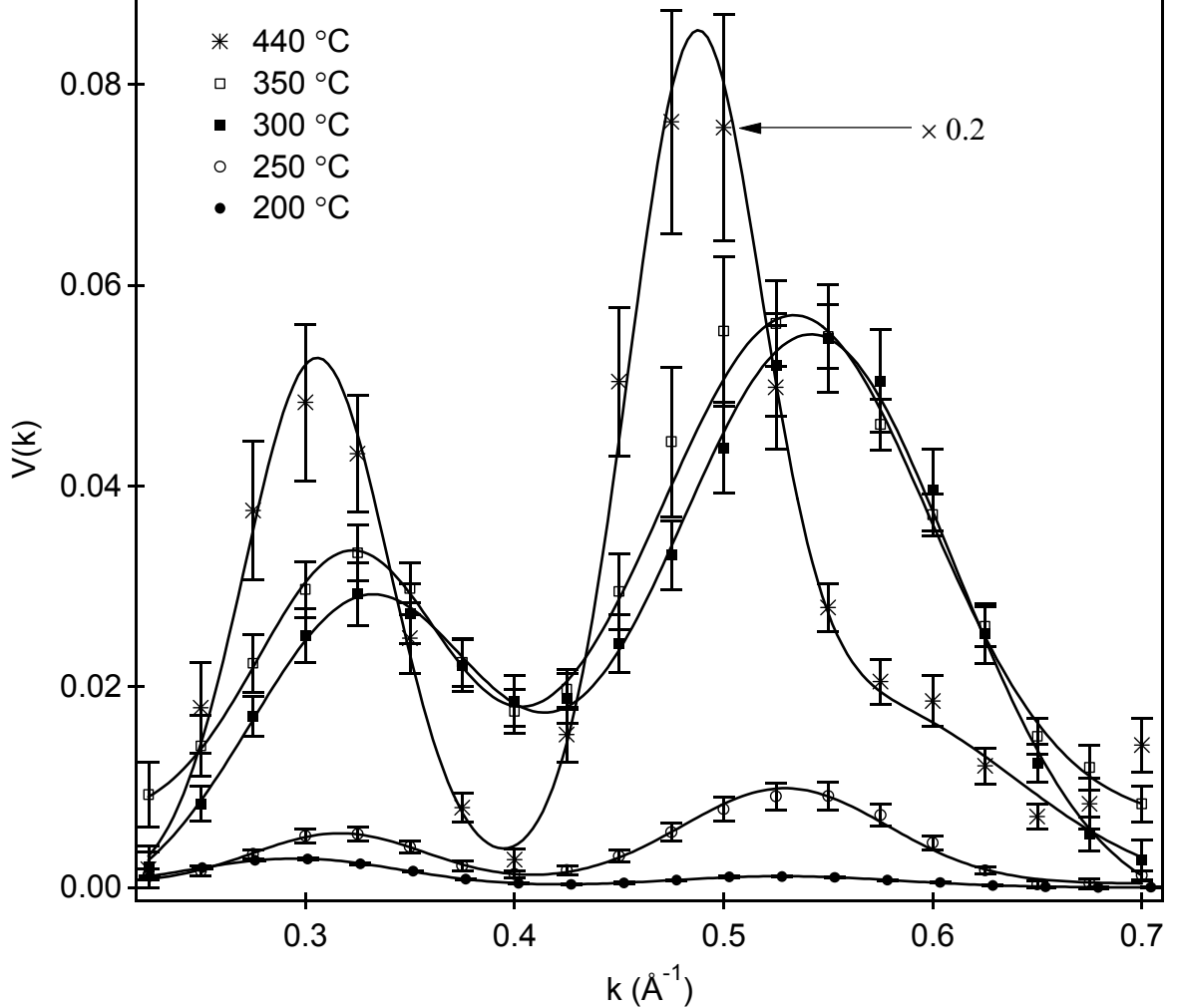


Figure 5:  $V(k)$  for magnetron sputtered a-Si films as a function of substrate temperature during growth. Note the continuous increase in variance with increasing temperature. Taken from Ref. [29].

In separate experiments, we increased by means of a magnetic field the flux of  $\text{Ar}^+$  ions to the growth surface at a constant substrate temperature of 230 °C; the ion energy was fixed at  $\sim 20$  eV so that the ion impacts would be able to displace surface atoms but not induce sub-surface vacancies [31]. As shown in Figure 6,  $V(k)$  increased monotonically as the ratio of ion flux to depositing Si atom flux (denoted neutral flux) was increased from 3 to 39; no nanocrystallites were detected.

Our results as a function of substrate temperature challenge the long standing view that a phase boundary separates amorphous and nanocrystalline silicon. This idea is based on experiments by Veprek *et al.* in which they deposited a-Si:H films using plasma CVD and analyzed the structure using x-ray diffraction [32]. Under various growth conditions, nanocrystals were never observed with a diameter below  $\sim 30$  Å, as determined by the Scherrer formula. They argued, in direct analogy with

nucleation theory, that smaller grains were not stable due to excess grain boundary energy. Our work suggests a different interpretation: suitable growth conditions can continuously increase the MRO in amorphous silicon up to size at which such order becomes *detectable* by x-ray diffraction or conventional TEM imaging: Veprek's experiments were dominated by a sharp cutoff in the sensitivity of x-ray diffraction to order, rather than by a thermodynamic boundary in the stability of such order. In Section 4, we will explain this sensitivity cutoff in detail.

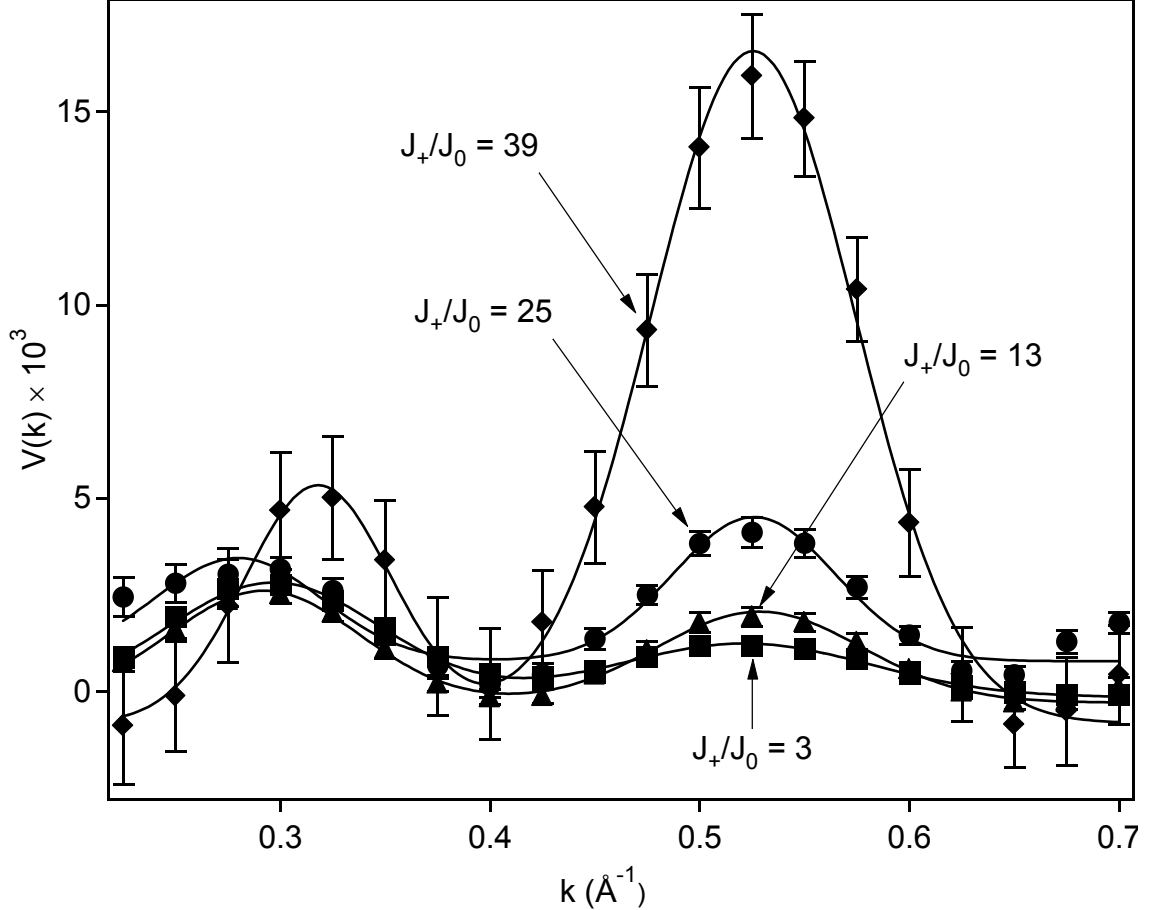


Figure 6:  $V(k)$  for magnetron sputtered a-Si films as a function of the flux ratio of low energy  $\text{Ar}^+$  ions ( $J^+$ ) to depositing Si atoms ( $J^0$ ) at a constant substrate temperature of  $230^\circ\text{C}$ . Note the continuous increase in variance with increasing ion flux. Taken from Ref. [30].

**3.3 Implant amorphized a-Si:** Cheng *et al.* showed that a-Si formed by ion self-implantation amorphization of c-Si wafers gives a high  $V(k)$  [27, 33]. Interestingly, the variance is almost identical to that of a magnetron sputtered a-Si film supplied by the Abelson group [33]. The implantation conditions used ( $\text{Si}^+$  ions in a double implant at 300 and 700 keV) produced a relatively flat energy dissipation and amorphization to a depth of  $1\ \mu\text{m}$ , and corresponded to the spike regime, in which local volumes of material are in effect melted and resolidified on a very rapid time scale. It is well established that thermal annealing of implant amorphized a-Si leads to a large heat release prior to recrystallization [34]. Cheng found that such annealing produced a decrease in  $V(k)$  towards that of a CRN, and interpreted, similar to the work of Gibson and Treacy on evaporated a-Ge, that the initial state with MRO is metastable with respect to a state that is closer to a CRN. In addition, FEM depth profiling revealed that  $V(k)$  for the as-implanted sample declined sharply  $\sim 0.7\ \mu\text{m}$

into the implant, where the calculated population of vacancies is high. This suggests that a large vacancy concentration may be able to promote the relaxation of MRO.

#### 4. Structural Models

As mentioned above, our primary method of interpreting the experimental results is to compare the variance data  $V(k)$  with simulations based on atomistic structural models [26, 35, 36]. We simulate dark-field TEM images from a collection of atomic coordinates using well-established techniques [37], then calculate  $V(k, Q)$  from the images. Electron microscopy image simulations tend to overestimate the contrast in real images [38], so the magnitude of the simulated variance is systematically too large compared to the data. *Relative* contrasts are much more reliable, so we rely on spectral patterns and relative feature sizes in  $V(k, Q)$ .

The first conclusion reached based on such simulations was that continuous random network models do not describe the MRO of real a-Si or a-Ge [26]. We have tested CRN computer models created by (i) quenching from a Si melt using the Stillinger-Weber potential [15] or the Biswas potential [39], (ii) models created by the Wooten-Winer-Weaire (WWW) bond-switching algorithm [40], and (iii) models created by the more recent Barkema-Mousseau refined WWW technique [41]. As shown in Figure 7, none of the CRN models show the characteristic double-peak structure observed in the experimental  $V(k)$  data discussed in the previous section [26, 36]. Instead, they show small modulations at random positions, the magnitude of which correlates more strongly with the total system size than any other variable. The size of these peaks give some measure of the uncertainty in the simulations created by the finite size of the CRN models.

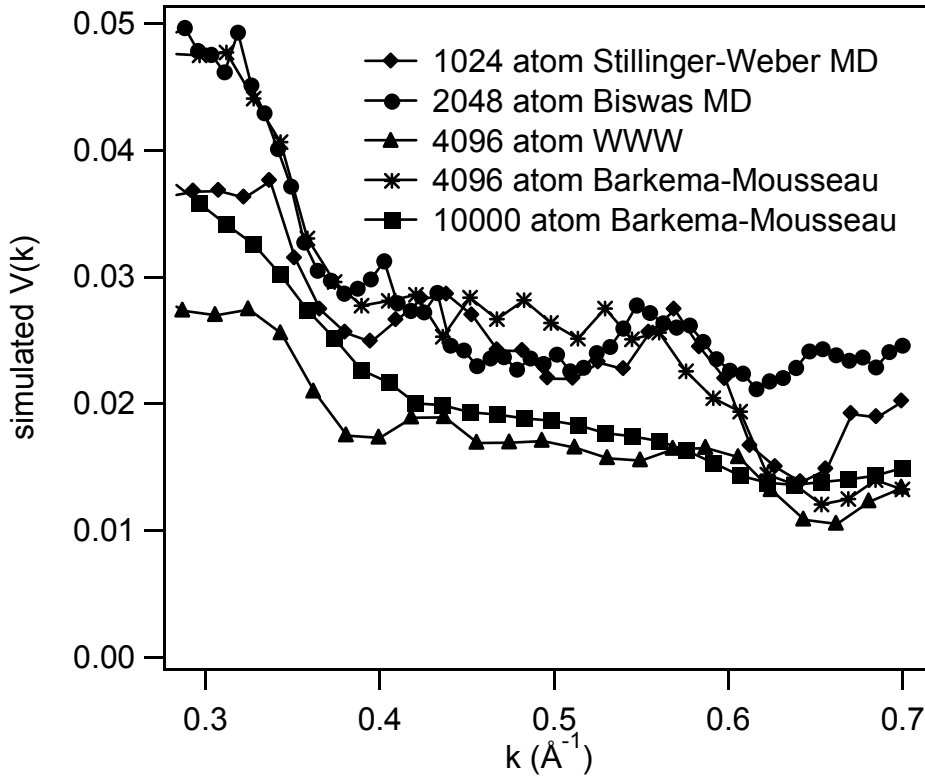


Figure 7:  $V(k)$  simulations for a several CRN models prepared using different energy minimization schemes, different system sizes, and different empirical potentials. None of them show the characteristic double-peak structure seen in the experimental data.



If not a CRN, then what? Treacy, Gibson and Keblinski proposed a *paracrystalline* (PC) structure [26] based on models originally developed by Keblinski to study the amorphous phase found at high-angle grain boundaries in Si [42]. Keblinski found that if he made the crystal grains in his grain boundary models very small, the calculated  $g_2(r)$  began to look more like an amorphous material than a crystal. In fact, Keblinski had found a synthesis path to creating a model consisting of very small crystalline grains embedded in a CRN matrix.

Simulated  $V(k)$  functions from Keblinski's three early models are shown in Figure 8. These models were synthesized using molecular dynamics by inserting four perfectly crystalline grains into an Si melt, cooling below the melting temperature with the grains intact, then allowing the system to relax [36]. The models vary in the size of and volume fraction occupied by the grains. This is an entirely unphysical synthesis route, but it resulted in models which have the characteristic double peaks in  $V(k)$  observed experimentally [26]. Despite the small size of the models, the peaks in  $V(k)$  are  $\sim 10$  times larger than the size-dependent structure observed in the CRN models.

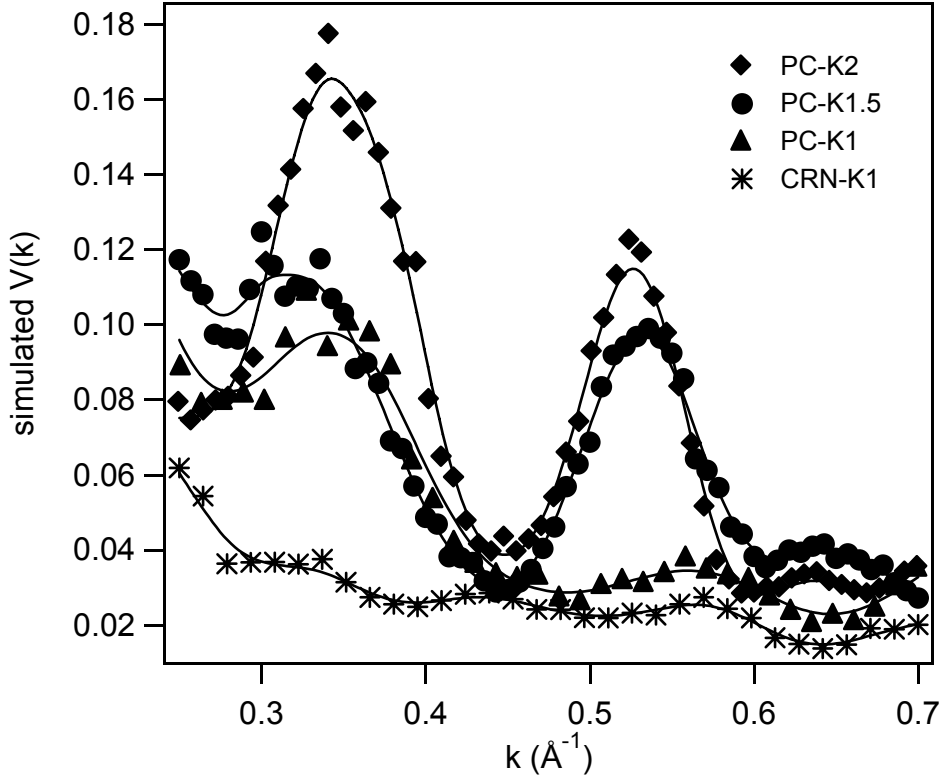


Figure 8:  $V(k)$  simulations for three early Keblinski paracrystalline structural models and the Stillinger-Weber CRN. In order from the largest, densest paracrystalline grains to the smallest, least dense grains, the models are: PC-K2, PC-K1.5, PC-K1, and CRN-K1. The smooth curves are a guide to the eye. Taken from Ref. [36].

As pointed out recently by Drabold [24], none of the model synthesis methods for amorphous materials is physically realistic; what matters is that the method naturally favor the atomic coordination which is known to exist on the final structure. MRO can then be studied in the context of a realistic short range order. The problem with melt-quench methods is that liquid Si has nearly 6-fold coordination, which is difficult to remove during  $\sim 1$  ps of simulated annealing. By contrast, the WWW method maintains 4-fold coordination by construction, which yields a physically realistic network. Moreover, it has been shown that the relaxation of a Si network *actually* involves bond switching events [43].

The calculated  $g_2(r)$  for the model with the least MRO also a good fit for the experimental  $g_2(r)$  measured by x-ray diffraction, as shown in Figure 9. (Models in which the grains are too large show extra peaks in  $g_2(r)$  that are not present in experiments on a-Si.) All the PC models are rendered *diffraction amorphous* by two factors. First, the grains occupy a relatively small volume fraction of the model, so their diffraction signature must compete with a significant background from the intergranular material. Second, the grain boundaries create a significant strain field in the ordered regions, extending at least 1 nm from the center of the boundary [42]. Once the strain fields from opposite boundaries of a grain overlap, there is no longer any unstrained material remaining. The grains remain topologically ordered in that no internal bonds are broken, but the strain significantly reduces the intensity of the Bragg peaks (in real space, smears out the sharp peaks in  $g_2(r)$ ).

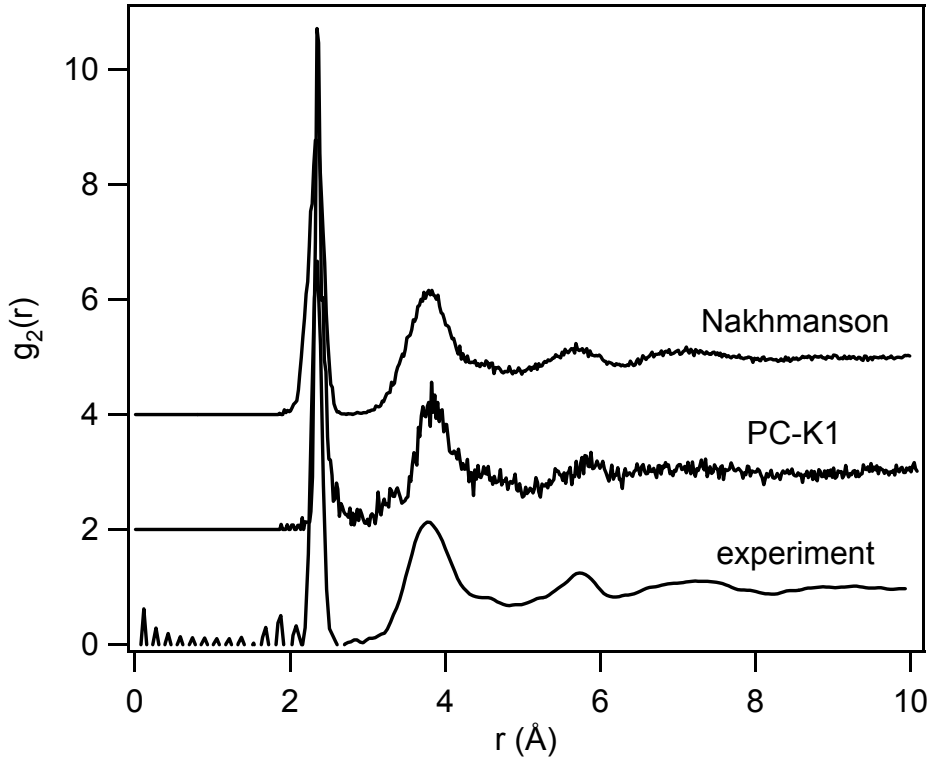


Figure 9:  $g_2(r)$  for the Koblinski model PC-K1 [26, 36] and a Nakhmanson PC model [35] compared to experimental data for a-Si measured by x-ray diffraction [5, 6]. Despite having significant MRO as shown in  $V(k)$ , the PC models are a good match for the experimental RDF.

All of the amorphous films which we have been examined to date – a-Ge, a-Si, and a-Si:H produced by various deposition methods, as well as a-Si produced by ion implantation of c-Si – exhibit clear peaks in  $V(k)$ . We therefore conclude that while the CRN is a useful ideal, representing a maximally disordered material, the paracrystalline structure is a better description of real tetrahedral amorphous semiconductors. At the same time, the intergranular regions in our models of paracrystalline Si appear to be a CRN in terms of their bond length, bond angle, and dihedral angle statistics [36]. Thus, even a material with the largest possible fraction of paracrystallites is expected to contain some CRN-like material.

The earliest Koblinski models [26] were synthesized using a melt-quench algorithm with the Stillinger-Weber potential, and had an unacceptably high concentration of coordination defects, approaching 50% in the worse cases. (This problem is shared by CRN models synthesized the same way [15].) Electronic structure calculations

showed that these models were almost metallic, they had so many states in the band gap [36]. This situation was greatly improved by employing the EDIP potential [44], which resulted in models with coordination defect densities as low as 10 % [36]. Interestingly, this change did not affect the simulated  $V(k)$  strongly, which indicates that FEM is relatively insensitive to short-range structure like dangling bonds.

Nakhmanson *et al.* [35, 45] later developed a PC synthesis method based on the WWW bond-switching algorithm. Crystalline grains were introduced into a random matrix while maintaining four-fold configuration. The structure was relaxed with WWW bond-switches. In the initial stages, bonds inside the grains were not allowed to switch. This produced PC models with perfect four-fold coordination by construction. The models then received a post-synthesis MD annealing with the EDIP potential without restrictions; this produced  $< 0.1\%$  coordination defects, indicating the as-synthesized models are a robust metastable configuration. These models show  $V(k)$  in the best agreement with experiment so far, a clean electronic band gap, a vibrational density of states in good agreement with inelastic neutron scattering measurements, and an acceptable  $g_2(r)$  [35]. This agreement with multiple experimental data sets, including FEM, suggests that these are the best currently extant models of a-Si without hydrogen.

To understand these models, we need a quantitative method to detect the presence and size of the paracrystalline grains *after* the synthesis by MD annealing or WWW bond switching. In particular, we need to determine whether the initial configuration of grains, which was introduced by hand into the model, is relatively stable thermodynamically, or whether some (or all) of the grains dissolve. Finding the grains after synthesis is difficult, primarily because the grains are heavily strained. We therefore turn to analysis of the bonding *topology*, which is relatively insensitive to the effects of strain. Atoms are considered bonded if they are within a certain distance of one another. We use a cutoff distance of 2.6 Å, which is 10 % longer than the crystalline distance of 2.35 Å; thus, even considerably strained bonds are considered intact.

The most common topological measure for a structure is the ring statistics [17]. A ring is the shortest closed path of bonds beginning and ending on the same atom. The size of the ring is simply the number of bonds it contains. In the context of the PC model, we are particularly interested in crystalline topology. Crystalline Si contains only six-member rings, but amorphous models contain 5- and 7-member rings as well.

Treacy, Voyles and Gibson [46, 47] have developed a more selective topological diagnostic than the ring statistics, the Schläfli cluster. Based on the local cluster concept of Mariani and Hobbs [48, 49], the Schläfli cluster of an atom is the collection of atoms and bonds involved in all the rings emanating from the central atom. The cluster is labeled by computing the size of the rings closing each pair of bonds emanating from the central atom. A c-Si atom has four bonds, therefore six pairs of bonds, each of which closes a six ring, so the label is  $6_2 \cdot 6_2 \cdot 6_2 \cdot 6_2 \cdot 6_2 \cdot 6_2$ . (This notation is due to the 18<sup>th</sup>-century mathematician Schläfli [50], therefore the Schläfli cluster.) The label is completed by the number of atoms in the cluster, so the c-Si cluster, shown in Figure 10, has the label  $6_2 \cdot 6_2 \cdot 6_2 \cdot 6_2 \cdot 6_2 \cdot 6_2 : 29$ .

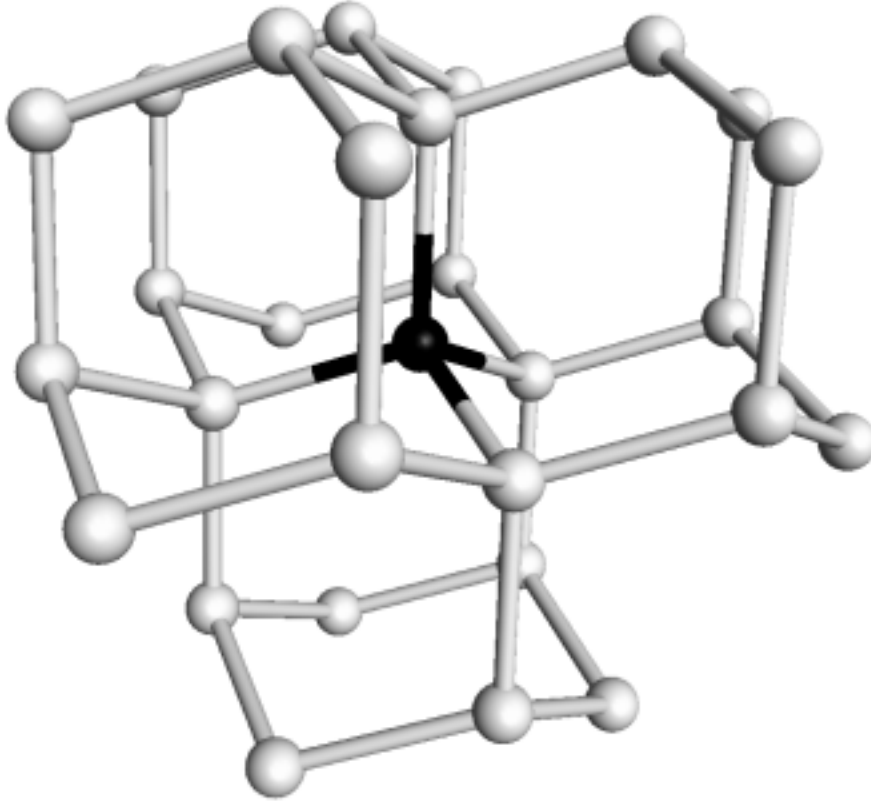


Figure 10: The  $6_2 \cdot 6_2 \cdot 6_2 \cdot 6_2 \cdot 6_2 \cdot 6_2 : 29$  Schläfli cluster of crystalline Si. The black atom is the center of the cluster. Each of the six pairs of bonds emanating from the central atom closes two six-rings, thus the label has  $6_2$  six times, and the cluster involves 29 atoms total.

Hobbs *et al.* have shown that all small-unit cell (i.e. excluding zeolites) four-connected crystals have uniquely labeled Schläfli clusters in this scheme [48]. We therefore define any atom with a Schläfli cluster found in a crystal as “topologically crystalline.” It is straightforward to calculate the Schläfli cluster for every atom in a given model, then search for topologically crystalline atoms, and connected groups of topologically crystalline atoms. We identify each connected group as a paracrystalline grain in our models.

The size and volume fraction of the paracrystalline grains provide a new and improved measure of MRO in models, and one which is well-correlated with the experimental results from FEM [36]. It is quite a strong measure of MRO, since none of the CRN models we have tested contains even one topologically crystalline atom. And, unlike correlated dihedrals or rings of a certain size, there is no pre-determined length scale – the connected clusters of topologically crystalline atoms can grow or shrink as the model demands.

Figure 11 shows the topologically crystalline grains in two of the Keglinski models, both of which started synthesis with 4 grains. In the model on the left, the initial grains contained 32 atoms and only two of the grains have survived the energy minimization. In the model on the right, the initial grains contained 64 atoms (the model is twice as large and the grains are farther apart), and all four grains have survived. Modeling studies are currently under way to examine the grain stability as a function of grain size, volume fraction, and packing; the results will allow us to bracket a region of paracrystalline grain stability (as limited by the constraints of the

relaxation method). Then, by comparing  $V(k, Q)$  simulations from these models to experimental data, we hope to further constrain the grain properties of the real material.

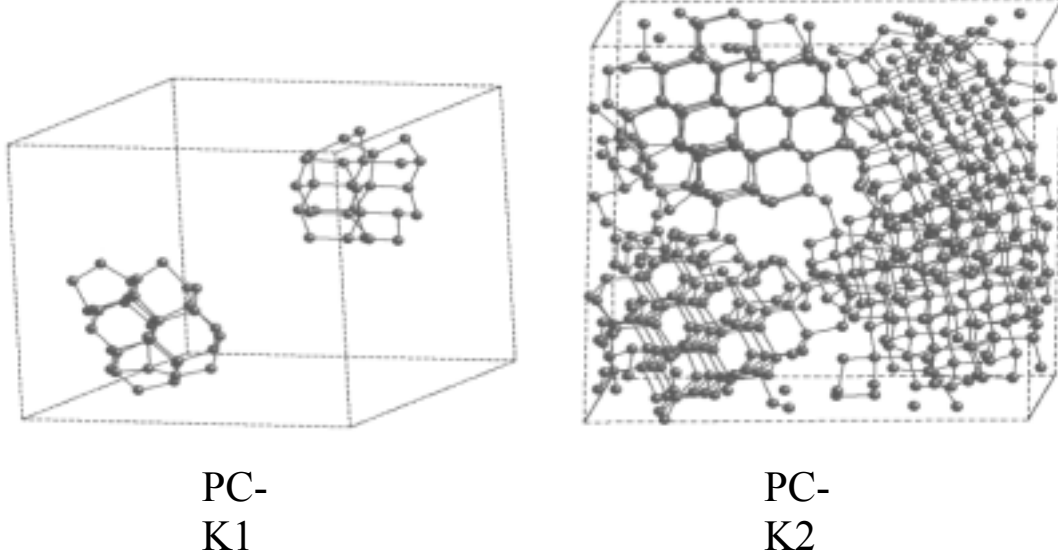


Figure 11: The topologically crystalline grains in models PC-K1 and PC-K2. Both models start synthesis with four crystalline grains. The starting grains in PC-K1 are smaller in size than in PC-K2, and only two of the grains in PC-K1 survive the energy minimization, while all four survive in PC-K2. Taken from Ref. [46].

From a thermodynamic viewpoint, it is interesting to regard the grains as nuclei which are predicted to dissolve below a critical size and to grow above it, just as in classical nucleation theory. Here, the excess free energy associated with the paracrystallite-CRN boundary also includes a significant strain field [26, 51]. Recent MD simulations of annealing have yielded evidence for just such a critical size: Bording and Taftø placed a grain of crystalline Ge in a matrix of a-Ge and found grain growth above a critical size of  $\sim 20$  Å and dissolution (back to a CRN) below it [52]; in a-Si, Nakhmanson observed crystallization events once nuclei of  $\sim 16$  Å diameter had formed [53]. These particle diameters are dependent on the details of the annealing simulations and should not be over-emphasized; still, both numbers fall exactly in the range of the paracrystallite sizes in our models and of the resolution ( $\sim 15$  Å) used in the FEM experiments that yield significant  $V(k)$ .

The structural models also allow us to understand and analyze the information from the FEM technique. Extensive analysis of the Keblinski models shows that the height of features in  $V(k)$  correlates with every other tested measure of MRO, such as correlations among dihedral angles, and the ratio of the transverse acoustic to transverse optical band intensities in the Raman spectrum and vibrational density of states [36]. The correlation length  $\Lambda$  extracted from the simulated  $V(Q)$  as suggested by Gibson, Treacy, and Voyles [22], has a monotonic correlation with all these quantities as well. Figure 12 shows that  $\Lambda$  is monotonic in the paracrystalline grain fraction of the model determined by Schläfli cluster analysis. This is particularly important because it makes a direct connection between the bonding topology and an experimentally measurable quantity.

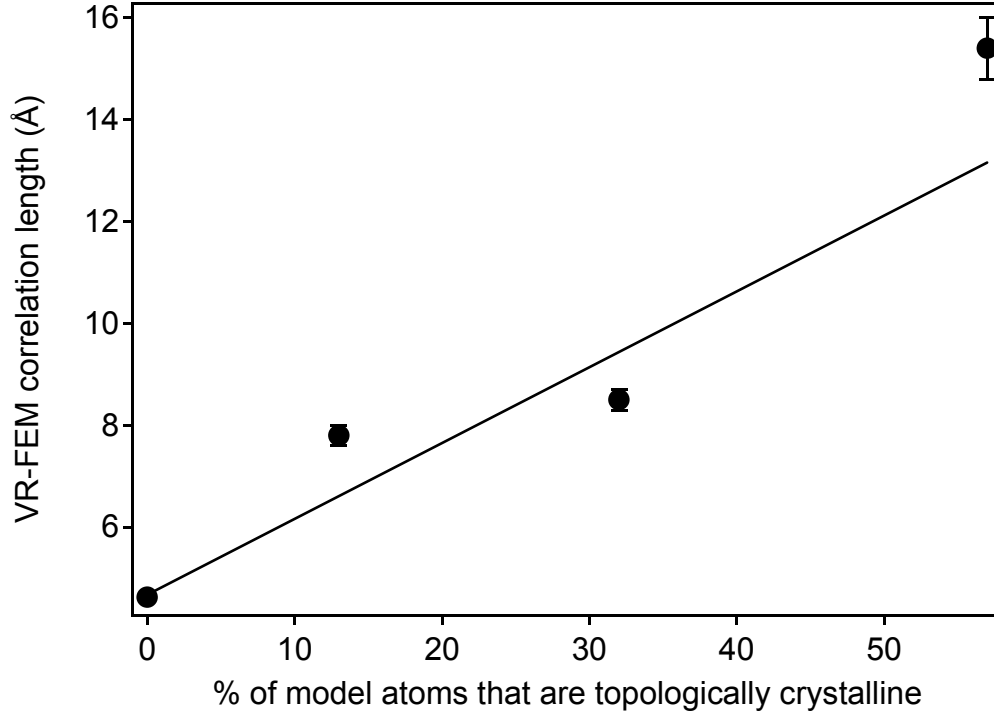


Figure 12: The simulated variable resolution correlation length  $L$  as a function of the percent of atoms in the model involved in the paracrystalline grains. The line is a linear fit given as a guide to the eye.

## 5. Experimental Results on a-Si:H and Discussion

We previously reported the variance  $V(k)$  of a-Si:H films deposited by plasma CVD (at the leading solar cell manufacturers United Solar Systems Corporation and BP Solar), by hot wire CVD [54] (at the National Renewable Energy Laboratory), by plasma CVD in the nanoparticle formation regime [55] (at the Ecole Polytechnique, Paris France) and by reactive magnetron sputtering [56] (in the Abelson laboratory at UIUC). The main conclusions of these earlier studies are that: (i) All films exhibit structure in  $V(k)$  and are therefore rich in MRO [57]. (ii) Despite the significant variation in growth fluxes – ranging from Si and H atoms to  $\text{SiH}_3$  radicals to Si:H nanoparticles –  $V(k)$  is more similar than it is different in all the resulting films. (iii) For a film deposited by reactive magnetron sputtering, light soaking reduces the first peak ( $k = 0.3 \text{ \AA}^{-1}$ ) in the  $V(k)$  signature by a factor of two [58].

The striking similarity in  $V(k)$  among the above films raises an essential issue: is the similarity the result of an energetic driving force in amorphous Si:H networks which tends to produce characteristic MRO? Or has the optimization of each process in terms of electronic quality led to a similar structure? The coupling between the MRO and electronic properties is not yet established; and, as discussed in Section 6 below, significantly more detailed information about MRO can be obtained using the variable resolution mode of FEM.

Here, we present recent results on two types of a-Si:H which reportedly contain locally ordered regions and have an enhanced resistance to light-induced degradation, with respect to ‘standard’ a-Si:H films. Figure 13 shows  $V(k)$  for a film grown at USSC by plasma CVD film with large  $\text{H}_2$  dilution of  $\text{SiH}_4$  (conditions near to the ‘edge’ of those which yield nanocrystallinity) [59] and for a film grown at the Ecole Polytechnique by plasma CVD with a high pressure of  $\text{SiH}_4$ , conditions that produce nanoparticles in the plasma (the ‘polymorphous’ regime) [60]. At first inspection, the materials appear to be nearly the same, although the  $V(k)$  peak for the polymorphous

film is higher. However, measurements on different areas reveal that these materials are spatially inhomogeneous, but in different ways.

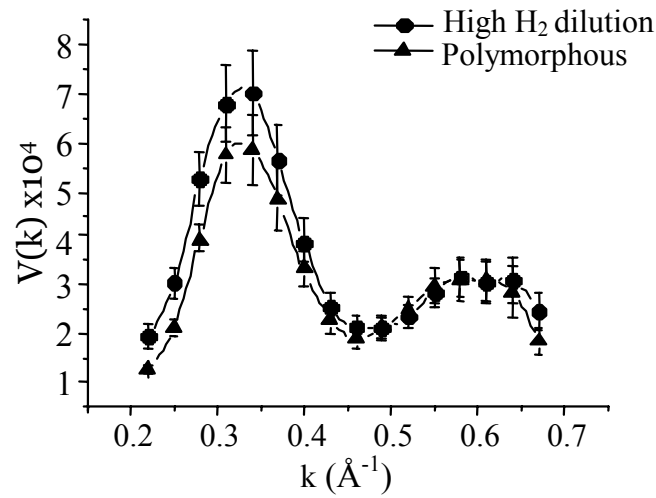


Figure 13:  $V(k)$  for a-Si:H films grown by plasma CVD (i) at USSC with large  $H_2$  dilution of  $SiH_4$  ('edge' material) and (ii) at the Ecole Polytechnique with a high pressure of  $SiH_4$  (the 'polymorphous' regime).

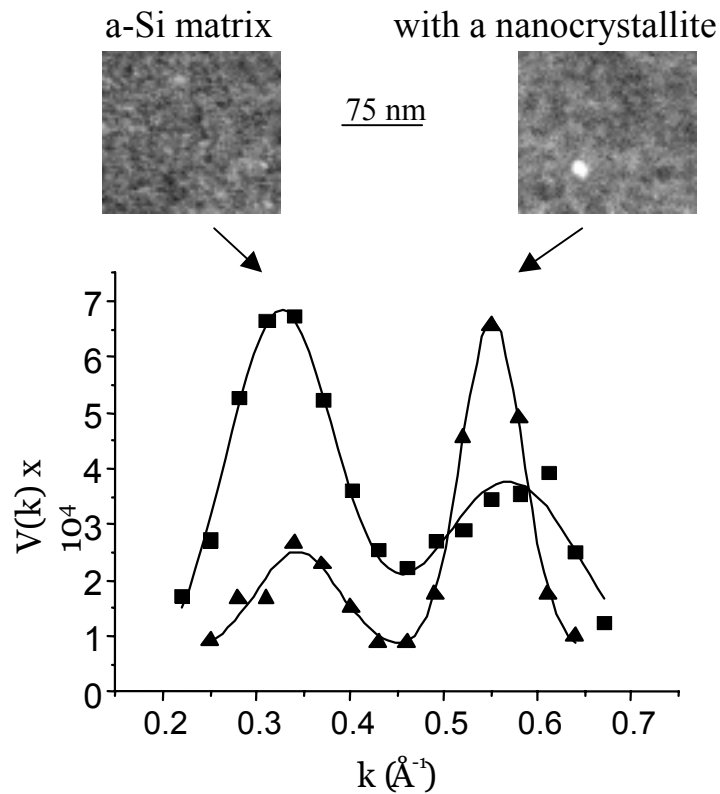


Figure 14: Dark field TEM images (for  $k = 0.55 \text{ \AA}^{-1}$ ) and the unaveraged  $V(k)$  traces for two different locations on the  $H_2$  diluted USSC film. The area on the left represents typical matrix a-Si:H material; the area on the right includes a nanocrystallite immersed in this matrix.

Figure 14 shows dark field images (for  $k = 0.55 \text{ \AA}^{-1}$ ) and the unaveraged  $V(k)$  traces for two different locations on the  $\text{H}_2$  diluted USSC film. The area on the left represents typical matrix a-Si:H material; the area on the right includes a large ( $\sim 10 \text{ nm}$ ) nanocrystallite immersed in this matrix, which greatly perturbs the variance data. (In all other instances, we only report  $V(k)$  data for the matrix, i.e. by averaging ten areas which are free of nanocrystallites.) This example illustrates the high sensitivity of FEM to the presence of nanocrystallites; by contrast, the search for small crystals in high resolution TEM images is fraught with difficulties [61]. Hollow-cone illumination is particularly useful for finding nanocrystals: it increases the number of Bragg conditions that make the nanocrystal appear bright, and if the image is viewed in real-time, the nanocrystal will flash as the beam sweeps around the cone. The use of  $\text{H}_2$  dilution has been observed to sharpen the x-ray ‘first sharp diffraction peak’ of a-Si:H, but this effect is due to the dilute population of nanocrystallites [62], rather than due to a change in the MRO of the matrix [57].

We also measured a USSC film which was deposited without the  $\text{H}_2$  dilution. The variance of the matrix was essentially identical to that of the film shown in Figure 13, however, no nanocrystallites were found in any of the images. Because the FEM data indicate no difference in the MRO of the a-Si:H matrix, the better electronic stability obtained with  $\text{H}_2$  dilution appears to be associated with the presence of the nanocrystallites [57]. Indeed, capacitance-based defect spectroscopies have found unique electronic transitions associated with nanocrystalline inclusions [63], and these transitions modify the early time kinetics of the SWE [64].

The polymorphous a-Si:H films are inhomogeneous in a different manner. Figure 15 shows individual  $V(k)$  traces from different areas of samples deposited using higher (left) and lower (right) pressures of  $\text{SiH}_4$  feedstock. At the higher pressure, which corresponds to a high electronic quality, there is a pronounced variation in the amplitude of  $V(k)$ . All amorphous samples, regardless of origin, exhibit area-to-area variations in FEM, but this particular sample is conspicuous because it has the largest variations which we have measured to date. Unlike the USSC film, no nanoparticles were detected. The presence of nanoparticles tends to increase the amplitude of the second peak in  $V(k)$ , but the first peak dominates in the polymorphous films. It is surprising, and not at all understood, why the variance of an image measuring  $50 \times 50 \text{ nm}$  should itself vary over the sample surface when the growth flux contains only units of few-atom dimensions. Nanodiffraction-based FEM may be necessary to provide detailed insight into the structure of polymorphous films.

**5.1 Stability of paracrystalline grains:** We [51] proposed that paracrystallites are formed when crystalline grains nucleate rapidly at the film growth surface but are constantly buried by newly-formed grains, which limits their size to a few nanometers. The formation of internal boundaries between the grains induces a strain state (as demonstrated by the MD models) which raises the energy of the system, such that the paracrystalline state is metastable. This assumes that the energy of a free surface – the nascent grain facing into vacuum – is less than that of an internal boundary. One may then ask how the paracrystallites will evolve if network relaxation is allowed kinetically: is there a critical size, analogous to nucleation theory, below which they will relax towards a CRN, and above which they will coarsen towards nanocrystalline grains? This hypothesis has some similarity to the ideas of Veprek, but in our model no real phase change is involved and the origin of the excess energy is related to the strain fields.



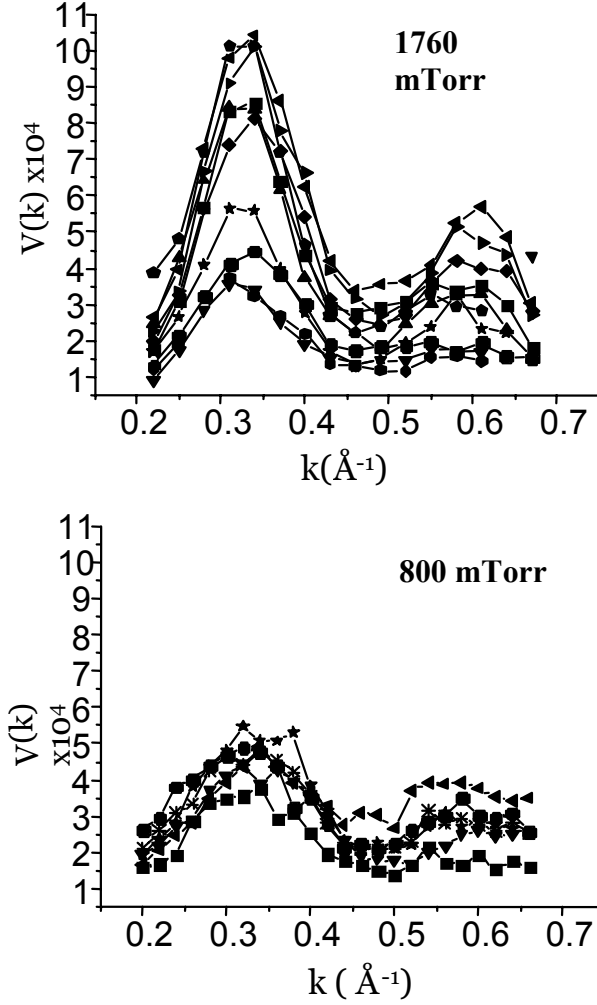


Figure 15: Unaveraged  $V(k)$  traces from different areas of samples of polymorphous a-Si:H deposited using higher (left) and lower (right) pressures of  $\text{SiH}_4$ . At the higher pressure, which corresponds to a high electronic stability, there is a pronounced spread in the amplitude of  $V(k)$  from area to area.

To test for network relaxation, Gerbi et al. [30] have explored the effect of implanting atomic H into the growing film during sputtering. Our in situ and computational studies of reactive magnetron sputtering using a plasma of  $\text{Ar} + \text{H}_2$  show that plasma-generated  $\text{H}_2^+$  ions are accelerated towards the Si target (cathode) and reflect from it as fast neutral H atoms which then impinge on the film in a broad distribution of kinetic energies, with a maximum of 200 eV and an average of  $\sim 100$  eV [56]. The H recoils shake Si atoms around with kicks of a few eV that should be sufficient to overcome configurational barriers, but the maximum energy transfer during a H-Si collision is, however, not sufficient to displace Si atoms (create vacancy-interstitial pairs as in c-Si).

Changing isotopes from H and D allows us to change the energy deposited in the film at constant flux and incident energy. Binary collision (TRIM) simulations for the reflection of  $\text{H}_2^+$  vs.  $\text{D}_2^+$  ions at the Si target surface show that neither the flux nor the energy distribution of the reflected fast neutrals (H vs. D) depends significantly on the isotope because of compensating effects during the multiple scattering process. In the growing film, however, the fast D atoms deposit twice as much energy as fast H

atoms, in the form of momentum-transfer recoils to a depth of  $\sim 50 \text{ \AA}$  [65]. The assumptions in the TRIM code remain valid down to a particle energy of  $\sim 10 \text{ eV}$  for H, which is sufficient.

Changing the isotope from  $\text{H}_2$  to  $\text{D}_2$  has significant effects on the MRO at constant substrate temperature [30]. In the regime of a-Si:H growth (low pressure of  $\text{H}_2$  or  $\text{D}_2$  injected into the plasma) the use of  $\text{D}_2$  *reduces* the variance  $V(k)$  as shown in Figure 16. The second peak ( $k = 0.55 \text{ \AA}^{-1}$ ) decreases much more than the first peak, such that the second peak dominates in a-Si:H and the first peak dominates in a-Si:D. Also, the first peaks shifts to slightly lower  $k$  using D. (Shifts in peak heights and positions are also visible in the a-Si substrate temperature series, Figure 5.) At present we cannot interpret these changes in a quantitative manner because we have not yet synthesized MD models with bonded hydrogen in order to simulate and match the FEM data, but such efforts are underway. The data clearly show, however, that the injection of kinetic energy into the subsurface of the growing film strongly modifies the paracrystalline structure.

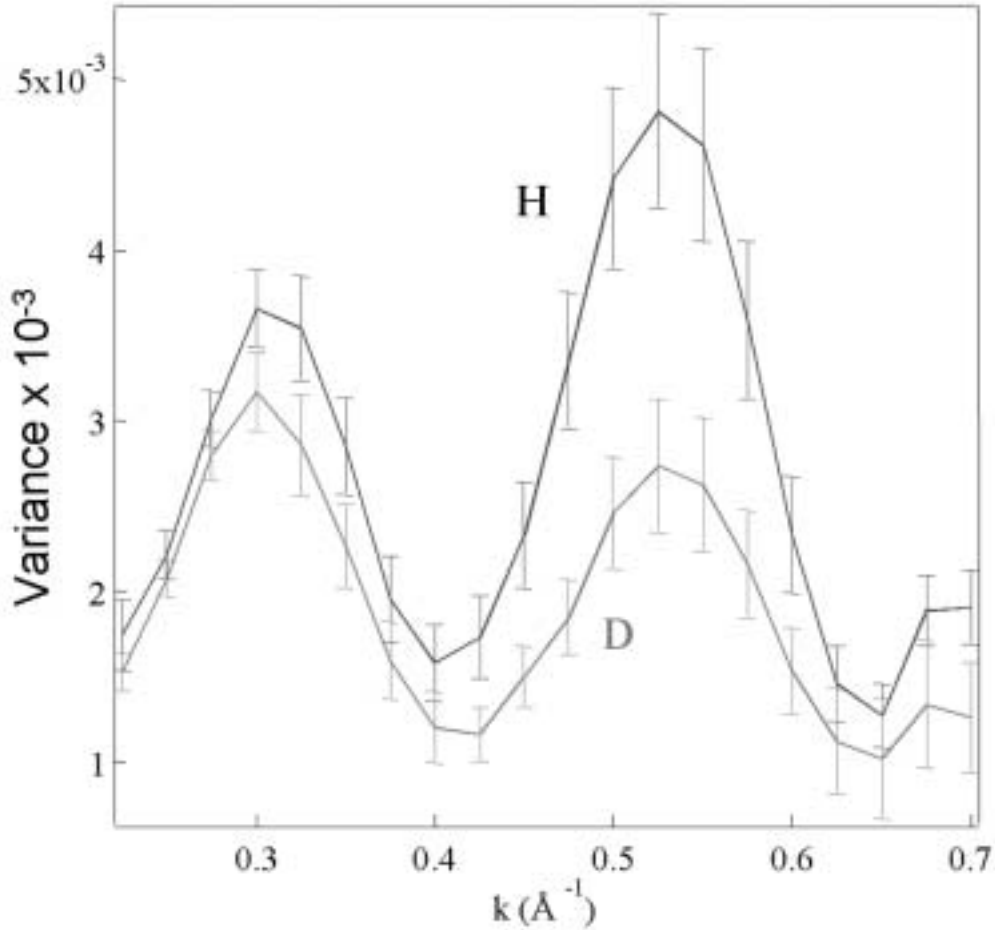


Figure 16:  $V(k)$  for a-Si:H grown by magnetron sputtering using either  $\text{H}_2$  or  $\text{D}_2$  injected into the plasma; the use of  $\text{D}_2$  *reduces* the variance  $V(k)$  due to increased momentum transfer to paracrystalline grains, which relax towards a CRN. Taken from Ref. [30].

By contrast, in the regime of nanocrystalline Si growth (high pressure of  $\text{H}_2$  or  $\text{D}_2$  injected into the plasma) the use of  $\text{D}_2$  *increases* the degree of nanocrystallinity, as we have shown using TEM, Raman, and spectroscopic ellipsometry measurements [66]. In related work, we showed that a flux of fast H atoms can transform a-Si:H into

nanocrystalline Si:H below the growth surface as soon as crystalline nuclei have formed [67].

These results are consistent with a critical stable grain size. In the a-Si:H growth regime, the paracrystallites are metastable and the network relaxes towards a CRN; in the nanocrystalline case, larger grains exist which are thermodynamically stable and tend to coarsen. To the extent that thermal H atoms supplied from the plasma can also facilitate network relaxation – by inserting into Si-Si bonds, which allows them to dilate – then similar effects can (and do!) occur during plasma CVD with H<sub>2</sub> dilution of SiH<sub>4</sub>.

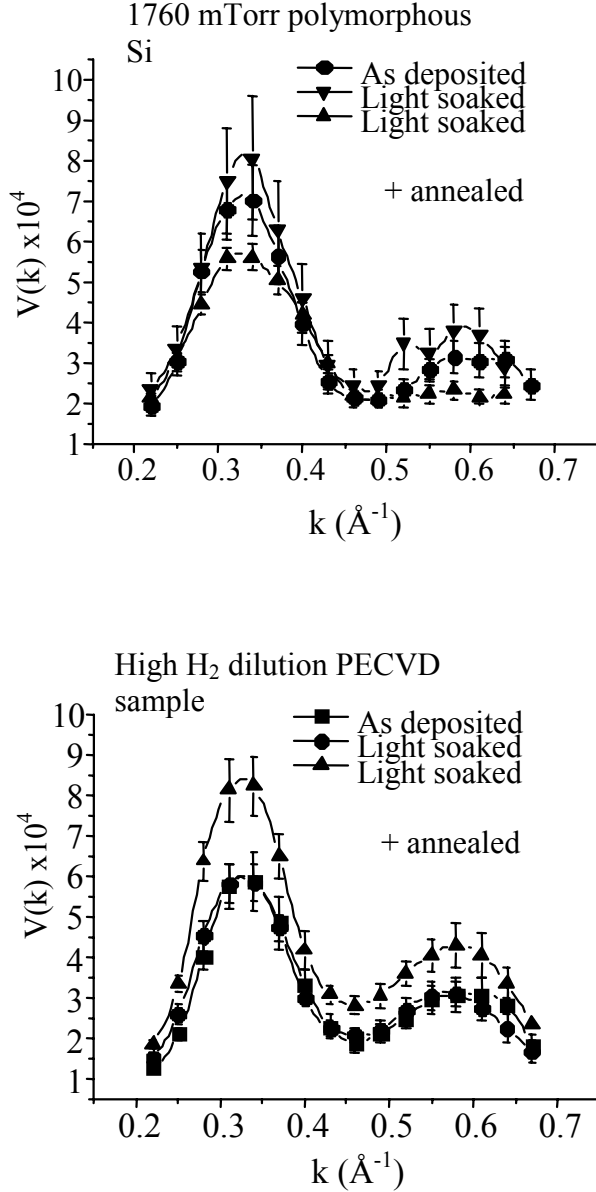


Figure 17:  $V(k)$  for the a-Si:H samples of Figure 12 in the as-deposited state, after light soaking (LS), and after light soaking plus thermal annealing (LS + AN); see text for experimental details. The changes are significant, and even the *sign* of the variance change can vary between films.

**5.2 Photostructural changes in a-Si:H:** A central issue in the science and technology of a-Si:H is the Staebler-Wronski Effect, i.e. the formation of metastable midgap electronic defects by prolonged exposure to above bandgap light or the injection of excess free carriers from doped contacts. As discussed extensively elsewhere in this volume, models of the SWE have traditionally been based on local defect reactions. However, recent experiments using IR absorption, NMR, XPS, and volume dilation show that structural relaxations also occur, which involve tens to thousands of Si atoms per defect created [68]. It is of great importance to understand the origin of these structural changes and their possible relationship with the creation of Si dangling bond defects.

We find that  $V(k)$  in the a-Si:H samples which are reportedly the most stable is modulated by a small but significant amount upon light soaking (projector bulb at 1.2 W/cm<sup>2</sup> for 200 hours, substrate maintained at 40°C) and subsequent thermal annealing (200°C for 1 hour in N<sub>2</sub>). Figure 17 shows the data for the H<sub>2</sub> dilution sample and the higher pressure polymorphous sample. Interestingly, even the *sign* of the variance change can vary between films, as we reported for preliminary light soaking experiments [23, 58].  $V(k)$  as we measure it is an average property of the whole sample. Even a large change in the positions of just a few atoms would not produce the effects we observe; a significant fraction of the atoms in the sample must be involved. Thus, our observations provide substantial evidence for changes in the microstructure of a-Si:H films as a function of light soaking. We hesitate to make a more specific interpretation until we can correlate the changes we detect with other structural probes and with the SWE. It will be critical to distinguish between the *reversible* portion of any changes in MRO and any irreversible relaxations from the as-deposited state.

It has been speculated that the a-Si:H network consists of two types of structural regions (which we will not refer to as phases), and that light soaking causes a small redistribution of atoms from one type to another [69]. In the context of the paracrystalline model, these regions would be the ordered grains and the matrix. Note that such modulation need not involve the long-range diffusion of Si atoms, only a change in bonding topology such that atoms leave the matrix and join the grains, or vice-versa, as in solid phase regrowth. This argument assumes that specific structural sites are causally related to the SWE, e.g., that the density of highly strained Si-Si bonds, which are the candidate sites for defect formation [70], varies with the modulations in the network. To support this line of thinking, it will be necessary to show that reversible changes occur in the MRO (or that similar changes can occur many times in the same sample) which correlate with the SWE defects; that such changes can be explained using reliable structural models and are consistent with other experimental data; and that the models predict a reversible change in the density of strained bonds.

In related work, Yu et al. found that exposure of a-Si to high doses of x-rays (up to 1 photon/atom at 4 keV) greatly delays the onset of solid phase crystallization when the samples are annealed at  $\geq 450^\circ\text{C}$ ; such a delay indicates that the sample has no pre-existing nuclei [71]. By contrast, samples which were not exposed began to crystallize immediately at high temperature, indicating the presence of nuclei. This work shows, empirically, that x-ray exposure can cause small ordered regions in the as-deposited material to relax towards an amorphous configuration.

## 6. Conclusions and Future Prospects

Using the technique of fluctuation electron microscopy, we have shown that medium range structural order exists in all samples of amorphous Si, Ge, and hydrogenated amorphous silicon which we have measured to date; these samples were grown using a variety of PVD and CVD techniques. The paracrystalline structural model, consisting of small, topologically ordered grains in an amorphous matrix, is consistent with the available data, including the fact that strain effects render this order invisible to diffraction measurements. We present data for different samples of hydrogenated amorphous silicon that reportedly have greater stability against the Staebler-Wronski effect. The matrix material of these samples is relatively similar, but the order changes in different ways upon both light soaking and thermal annealing. These samples are also inhomogeneous, having either nanocrystalline inclusions or larger area-to-area variation in the medium range order.

**6.1 Implications of the paracrystalline model:** All of the samples which we have measured contain MRO, which we have ascribed to paracrystallites. This raises the question, does the order have significant new ramifications, or does it simply represent a more detailed description of the structure, with all other properties unchanged? We have two answers.

First, the paracrystalline model is proving to be essential for explaining the details of electronic transport in a-Si:H. Drabold recently calculated the conduction band tail states in a paracrystalline model of a-Si and found them to be spatially located at the grain boundaries [2]. This implies an aspect of percolation in the transport problem; percolation has also been invoked to explain the noise power spectrum [72]. Of course, it is crucial to determine if the conduction band tail states have a similar spatial distribution in hydrogenated a-Si:H, which requires the development of a suitably large and reliable atomic model.

Second, our current FEM experiments function mainly at the level of fingerprinting and comparison: a given sample has more or less MRO than another. Future work using nanodiffraction on the STEM to obtain fluctuation maps  $V(k, Q)$  will better elucidate and quantify the structural differences between samples as a function of the growth method, light soaking, and thermal annealing. MRO has a rich phenomenology: in our variable coherence data, the  $V(k)$  peaks change not only in amplitude but in relative height and in peak position. However, the use of a fixed  $Q$  makes these data less sensitive to MRO on lengths scales far from  $1/Q$ . Detailed interpretation will also require a suitable set of MD models in order to compare simulated and measured data. Once identified and correlated with the SWE this detailed understanding of MRO can guide film growth efforts towards improved properties, especially stability. In our view, it is fundamentally unclear whether the most stable a-Si:H film will involve a minimum or maximum in the MRO. Future work may shed light on other unresolved issues involving the structure, such as the lack of the internal friction signature otherwise universal to amorphous materials in a-Si:H films deposited by hot wire CVD [73].

**6.2 Depth dependence of MRO:** FEM measurements must be performed on a freestanding film only  $\sim 200$  Å thick. All the films discussed above were deposited to this thickness on Al foil or NaCl substrates; the substrates were then dissolved off and the flakes captured on Cu TEM sample grids. Our work to date has not tested for the possible influence of the substrate material on the MRO, or the evolution of MRO as a function of film thickness. Interface effects are presumably not large because the nucleation and coalescence of a-Si:H on most substrates is complete by a thickness of

$\sim 20 \text{ \AA}$ , and is followed by the growth of material with “bulk” properties. Recently, a differential thinning method for Si films has been developed [27] which permits the evaluation of a  $\sim 200 \text{ \AA}$  thick slice located at arbitrary depth within the sample. This technique, in possible combination with cross-sectional sample preparation, will allow us to test for internal variations in MRO. Interesting possible studies include MRO in a-Si:H near to the a-SiN<sub>x</sub>:H interface in thin film transistors, or as a function of position in p-i-n solar cells, or at the boundary between amorphous and nanocrystalline layers.

**6.3 Study of amorphous alloys:** The FEM technique is also applicable to amorphous alloy films such as silicon nitride or silicon carbide. We fully expect that these materials will show both MRO and spatial variations in the experimental data. As in the case of amorphous silicon, interpretation of the data requires that we synthesize reliable structural models in the computer, simulate the FEM data, and iteratively match with experiment. However, the generation of such models is a challenging undertaking, the more so because the useful electronic materials contain bonded hydrogen and are therefore ternary alloys. Still, the FEM data should increase monotonically with the degree of MRO and will elucidate any major trends.

**6.4 Variable resolution FEM using nanodiffraction:** The next main development in the FEM technique will be implementing FEM measurements via nanodiffraction instead of dark-field imaging. In this mode, the  $I(\mathbf{r}, \mathbf{k}, Q)$  data set is collected by using the electron microscope lenses to form a nanometer-diameter electron probe, positioning it on the sample, and collecting data with an angle-resolved detector in a diffraction plane.  $\mathbf{r}$  is changed by moving the probe, and all of the  $\mathbf{k}$  data for a given  $\mathbf{r}$  are collected simultaneously.  $Q$  is then related to the convergence angle of the probe. The ray diagram looks like Figure 2 turned upside down.

Nanodiffraction has several advantages: first, because we collect essentially all of the scattering from every probe position, it should be a more efficient use of the electron dose to the sample. Since damage from the keV electron beam is always a concern, minimizing the dose to the sample is important [58]. Second, it is much easier to collect data systematically as a function of scattering vector  $\mathbf{k}$  instead of vector magnitude  $k$ . This will allow us to test directly for anisotropy in the MRO. Third and most important, in this imaging mode it is possible to vary  $Q$  electronically instead of mechanically using the virtual objective aperture in the scanning TEM. This opens the possibility of doing systematic variable resolution FEM experiments, and raising the level of quantification of FEM. Nanodiffraction also holds the best possibility for collecting full fluctuation map data sets,  $V(\mathbf{k}, Q)$ , which will give us the maximum possible information about MRO.

Some initial results on nanodiffraction FEM have been achieved [20, 74]. Voyles and Muller [20] formed a coherent probe whose FWHM could be varied smoothly from 0.8 to 5 nm, and demonstrated that (i) the nanodiffraction pattern from an a-Si sample varies significantly as a function of probe size and of spatial position on the sample; (ii) the  $V(k)$  data obtained using the scanning TEM agree quantitatively with those obtained using hollow-cone illumination in a conventional TEM; the  $V(k)$  data for an a-Ge sample are significantly modified by a change in probe size from 1.0 and 2.6 nm. These constitute a proof of principle, and we expect to acquire and analyze  $V(k, Q)$  fluctuation maps in the near future.

These initial results indicate some drawbacks as well. In particular, nanodiffraction FEM is more sensitive to the stochastic noise in the electron beam, making it more difficult to achieve adequate counting statistics. Nanodiffraction FEM also inevitably

measures fewer spatial samples than dark-field imaging FEM, which may make it less sensitive to very small differences in MRO.

**6.5 Other methods for characterizing MRO:** Nor is FEM the last word on characterizing MRO in amorphous materials with the electron microscope. McBride *et al.* [75] recently reported a methodology for measuring  $g_2(r)$  from small volumes; systematic variations in  $g_2(r)$  from place to place could be a measure of MRO. Motivated by the development of FEM, Cowley [76, 77] has proposed a number of possible variations using nanodiffraction to study MRO; these include analyzing the persistence of spots in the diffraction pattern as the probe is moved across the sample, and scanning TEM imaging using a thin annular detector. These ideas await further development (as does FEM), but seem likely to reveal additional information about MRO in amorphous materials.

## **Acknowledgments**

A great many researchers have contributed to their work and ideas to what we have presented here. We are particularly grateful to J. M. Gibson and M. M. J. Treacy, the inventors of FEM, and to P. M. Voyles, who brought the technique to fruition and collaborated *extensively* with our group in both experiment and interpretation. We also thank P. Keblinski, D. A. Drabold, and S. Nakhmanson for many helpful discussions.

Portions of the research were carried out in the Center for Microanalysis of Materials, University of Illinois, which is supported by the U. S. Department of Energy under grant DOE DEFG02-91ER45439.



## References

- [1] W. H. Zachariasen, *J. Am. Chem. Soc.* 51 (1932) 3841.
- [2] J. Dong, D. A. Drabold, *Phys. Rev. Lett.* 80 (1998) 1928.
- [3] B. R. Djordjevic, M. F. Thorpe, F. Wooten, *Phys. Rev. B* 52 (1995) 5685.
- [4] B. E. Warren, *X-ray Diffraction* (Addison-Wesley, Reading, 1969) p. 136.
- [5] K. Laaziri, S. Kycia, S. Roorda, M. Chicoine, J. L. Robertson, J. Wang, S. C. Moss, *Phys. Rev. B* 60 (1999) 13520.
- [6] K. Laaziri, S. Kycia, S. Roorda, M. Chicoine, J. L. Robertson, J. Wang, S. C. Moss, *Phys. Rev. Lett.* 82 (1999) 3460.
- [7] R. Bellissent, A. Chenevas-Paule, M. Roth, *J. Non-Cryst. Sol.* 59-60 (1983) 229.
- [8] A. Menelle, *J. Non-Cryst. Sol.* 97-98 (1987) 337.
- [9] D. L. Williamson, *Mat. Res. Symp. Soc. Proc.* 377 (1995) 251.
- [10] J. Baugh, D. Han, A. Kleinhammes, Y. Wu, *Appl. Phys. Lett.* 78 (2001) 466.
- [11] A. D. Cicco, A. Bianconi, C. Coluzza, R. Rudolf, *J. Non-Cryst. Sol.* 116 (1990) 27.
- [12] M. Benfatto, A. Bianconi, I. Davoli, J. Garcia, A. Marcelli, C. R. Natoli, S. Stizza, *J. Non-Cryst. Sol.* 77-78 (1985) 1325.
- [13] A. P. Sokolov, A. P. Shebanin, *Sov. Phys. Semicond.* 24 (1990) 720.
- [14] G. Morell, R. S. Katiyar, S. Z. Weisz, J. Jia, J. Shinar, I. Balberg, *J. Appl. Phys.* 78 (1995) 5120.
- [15] W. D. Luedtke, U. Landman, *Phys. Rev. B* 40 (1989) 1164.
- [16] S. R. Elliott, *Adv. Phys.* 38 (1989) 1.
- [17] S. V. King, *Nature* 213 (1967) 1112.
- [18] M. M. J. Treacy, J. M. Gibson, *Acta Cryst A* 52 (1996) 212.
- [19] P. M. Voyles, M. M. J. Treacy, J. M. Gibson, H.-C. Jin, J. R. Abelson, in J. Bentley, U. Dahmen, C. Allen, I. Petrov, ed., *Advances in Materials Problem Solving with the Electron Microscope* (Materials Research Society 589, San Francisco, 2001) 155.
- [20] P. M. Voyles, D. A. Muller, *Ultramicroscopy* 93 (2002) 147.
- [21] P. M. Voyles, J. M. Gibson, M. M. J. Treacy, *J. Electron Microscopy* 49 (2000) 259.
- [22] J. M. Gibson, M. M. J. Treacy, P. M. Voyles, *Ultramicroscopy* 83 (2000) 169.
- [23] P. M. Voyles, *Fluctuation Electron Microscopy of Medium-Range Order in Amorphous Silicon*, Ph. D. dissertation University of Illinois at Urbana-Champaign, 2001.
- [24] D. Drabold, J. Li, *Current Opinion in Solid State and Materials Science* 5 (2001) 509.
- [25] J. M. Gibson, M. M. J. Treacy, *Phys. Rev. Lett.* 78 (1997) 1074.
- [26] M. M. J. Treacy, J. M. Gibson, P. J. Keblinski, *J. Non-Cryst. Sol.* 231 (1998) 99.
- [27] J.-Y. Cheng, Ph. D. dissertation University of Illinois at Urbana-Champaign, 2002.
- [28] P. M. Voyles, J. E. Gerbi, M. M. J. Treacy, J. M. Gibson, J. R. Abelson, *J. Non-Cryst. Sol.* 293-295 (2001) 45.
- [29] P. M. Voyles, J. E. Gerbi, M. M. J. Treacy, J. M. Gibson, J. R. Abelson, *Phys. Rev. Lett.* 86 (2001) 5514.

- [30] J. E. Gerbi, P. M. Voyles, M. M. J. Treacy, J. M. Gibson, W. C. Chen, B. J. Hauser, J. R. Abelson, in J. B. B. e. al, ed., (Materials Research Society 664, San Francisco, 2001) A27.3.1.
- [31] M. Kitabatake, J. E. Greene, *Thin Solid Films* 272 (1996) 271.
- [32] S. Veprek, Z. Iqbal, F.-A. Sarott, *Phil. Mag. B* 45 (1982) 137.
- [33] J.-Y. Cheng, J. M. Gibson, D. C. Jacobson, *J. Mat. Res.* 16 (2001) 3030.
- [34] S. Roorda, S. Doorn, W. C. Sinke, P. M. L. O. Scholte, E. v. Loenen, *Phys. Rev. Lett.* 62 (1989) 1880.
- [35] S. M. Nakhmanson, P. M. Voyles, N. Mousseau, G. T. Barkema, D. A. Drabold, *Phys. Rev. B* 63 (2001) 235207.
- [36] P. M. Voyles, N. Zotov, S. M. Nakhmanson, D. A. Drabold, J. M. Gibson, M. M. J. Treacy, P. Keblinski, *J. Appl. Phys.* 90 (2001) 4437.
- [37] E. J. Kirkland, *Advanced Computing in Electron Microscopy* (Plenum, New York, 1998).
- [38] C. B. Boothroyd, *J. Microsc.* 190 (1998) 99.
- [39] R. Biswas, G. S. Grest, C. M. Soukoulis, *Phys. Rev. B* 36 (1987) 7437.
- [40] F. Wooten, K. Winer, D. Weaire, *Phys. Rev. B* 54 (1985) 1392.
- [41] G. T. Barkema, N. Mousseau, *Phys. Rev. B* 62 (2000) 4985.
- [42] P. Keblinski, S. R. Phillpot, D. Wolf, H. Gleiter, *Phys. Rev. Lett.* 77 (1996) 2965.
- [43] N. Mousseau, G. T. Barkema, *Phys. Rev. B* 61 (2000) 1898.
- [44] M. Z. Bazant, E. Kaxiras, J. F. Justo, *Phys. Rev. B* 56 (1997) 8542.
- [45] S. M. Nakhmanson, N. Mousseau, G. T. Barkema, P. M. Voyles, D. A. Drabold, *Int. J. Mod. Phys. B* 15 (2001) 3253.
- [46] M. M. J. Treacy, P. M. Voyles, J. M. Gibson, *J. Non-Cryst. Sol.* 266 (2000) 150.
- [47] M. M. J. Treacy, P. M. Voyles, J. M. Gibson, in H. M. Branz, R. W. Collins, S. Guha, H. Okamoto, M. Stutzman, ed., *Amorphous and Heterogeneous Silicon Thin Films 2000* (Materials Research Society 609, San Francisco, 2000) A2.5.1.
- [48] L. W. Hobbs, C. E. Jesurum, V. Pulim, B. Berger, *Phil. Mag. A* 78 (1998) 679.
- [49] C. S. Marians, L. W. Hobbs, *J. Non-Cryst. Sol.* 124 (1990) 242.
- [50] M. O'Keeffe, *Z. Kristallogr.* 196 (1991) 21.
- [51] P. M. Voyles, M. M. J. Treacy, J. M. Gibson, in H. N. Wadley, G. Gilmer, W. Barker, ed., *New Methods, Mechanisms, and Models of Vapor Deposition* (Materials Research Society 616, San Francisco, 2000) 47.
- [52] J. K. Bording, J. Taftø, *Phys. Rev. B* 62 (2000) 8098.
- [53] S. M. Nakhmanson, N. Mousseau, *J. Phys: Condens. Mat.* 14 (2002) 6627.
- [54] A. H. Mahan, B. P. Nelson, S. Salamon, R. S. Crandall, *J. Non-Cryst. Sol.* 137 (1991) 657.
- [55] P. R. i. Cabarrocas, S. Hamma, S. N. Sharma, G. Viera, E. Bertran, J. Costa, *J. Non-Cryst. Sol.* 227-230 (1998) 871.
- [56] J. R. Abelson, *Applied Physics A* 56 (1993) 493.
- [57] P. M. Voyles, M. M. J. Treacy, H.-C. Jin, J. R. Abelson, J. M. Gibson, J. Yang, S. Guha, R. S. Crandall, in H. M. Branz, R. W. Collins, S. Guha, H. Okamoto, M.

- Stutzman, ed., Amorphous and Heterogeneous Silicon Thin Films 2000 (Materials Research Society 609, San Francisco, 2000) A2.4.1.
- [58] J. M. Gibson, M. M. J. Treacy, P. M. Voyles, H.-C. Jin, J. R. Abelson, Appl. Phys. Lett. 73 (1998) 3093.
- [59] D. V. Tsu, B. S. Chao, S. R. Ovshinsky, S. Guha, J. Yang, Appl. Phys. Lett. 71 (1997) 1317.
- [60] C. Longeaud, J. P. Kleider, M. Gauthier, R. Bruggemann, Y. Poissant, P. R. I. Cabarrocas, in H. M. Branz, R. W. Collins, H. Okamoto, S. Guha, R. Schropp, ed., Amorphous and Heterogeneous Silicon Thin Films: Fundamentals to Devices - 1999 (Materials Research Society 557, San Francisco, 1999) 501.
- [61] J. M. Gibson, in T. Mulvey, ed., Electron Microscopy and Microanalysis 1979 (Institute of Physics Bristol, UK, 1979) 273.
- [62] A. H. Mahan, J. Yang, S. Guha, D. L. Williamson, Phys. Rev. B 61 (2000) 1677.
- [63] D. Kwon, C.-C. Chen, J. D. Cohen, H.-C. Jin, E. Hollar, I. K. Robertson, J. R. Abelson, Phys. Rev. B 60 (1999) 4442.
- [64] Y. Lubianiker, J. D. Cohen, H.-C. Jin, J. R. Abelson, Phys. Rev. B 60 (1999) 4434.
- [65] J. E. Gerbi, Appl. Phys. Lett. (under review).
- [66] J. E. Gerbi, P. M. Voyles, J. M. Gibson, J. R. Abelson, in R. Schropp, H. M. Branz, M. Hack, I. Shimizu, S. Wagner, ed., Amorphous and Microcrystalline Silicon Technology - 1998 (Materials Research Society 507, 1998) 429.
- [67] Y. H. Yang, M. Katiyar, N. Maley, J. R. Abelson, Appl. Phys. Lett. 65 (1994) 1769.
- [68] H. Fritzsche, in ed., Proc. MRS Symp. A 1997).
- [69] J. Baugh, D. Han, Phys. Rev. B 66 (2002) 1115203.
- [70] K. Winer, L. Ley, (World Scientific Pub., Singapore, 1989) p. 365.
- [71] K. M. Yu, L. Wang, W. Walukiewicz, S. Muto, S. McCormick, J. R. Abelson, in S. Wagner, M. Hack, E. A. Schiff, R. Schropp, I. Shimizu, ed., Amorphous and Microcrystalline Silicon Technology - 1997 (Materials Research Society 467, San Francisco, 1997) 355.
- [72] D. Quicker, P. W. West, J. Kakalios, J. Non-Cryst. Sol. 266-269 (2000) 397.
- [73] X. Liu, J. B. E. White, R. O. Pohl, E. Iwanizcko, K. M. Jones, A. H. Mahan, B. N. Nelson, R. S. Crandall, S. Veprek, Phys. Rev. Lett. 78 (1997) 4418.
- [74] J. M. Rodenburg, in ed., EMAG99 (IOP Publishing Ltd. Inst. Phys. Conf. Ser. 161, Sheffield, 1999) 145.
- [75] W. E. McBride, D. J. H. Cockayne, C. M. Goringe, Ultramicroscopy 76 (1999) 115.
- [76] J. M. Cowley, J. Electron Microscopy 50 (2001) 147.
- [77] J. M. Cowley, Ultramicroscopy 90 (2002) 197.

<b>REPORT DOCUMENTATION PAGE</b>			<i>Form Approved</i> OMB NO. 0704-0188	
Public reporting burden for this collection of information is estimated to average 1 hour per response, including the time for reviewing instructions, searching existing data sources, gathering and maintaining the data needed, and completing and reviewing the collection of information. Send comments regarding this burden estimate or any other aspect of this collection of information, including suggestions for reducing this burden, to Washington Headquarters Services, Directorate for Information Operations and Reports, 1215 Jefferson Davis Highway, Suite 1204, Arlington, VA 22202-4302, and to the Office of Management and Budget, Paperwork Reduction Project (0704-0188), Washington, DC 20503.				
1. AGENCY USE ONLY (Leave blank)	2. REPORT DATE October 2003	3. REPORT TYPE AND DATES COVERED Subcontract Report 23 June 1999–23 August 2002		
4. TITLE AND SUBTITLE Medium-Range Order in Amorphous Silicon Measured by Fluctuation Electron Microscopy: Final Report, 23 June 1999–23 August 2002		5. FUNDING NUMBERS PVP32601 AAD-9-18668-04		
6. AUTHOR(S) P.M. Voyles and J.R. Abelson				
7. PERFORMING ORGANIZATION NAME(S) AND ADDRESS(ES) University of Illinois at Urbana-Champaign Urbana, Illinois		8. PERFORMING ORGANIZATION REPORT NUMBER		
9. SPONSORING/MONITORING AGENCY NAME(S) AND ADDRESS(ES) National Renewable Energy Laboratory 1617 Cole Blvd. Golden, CO 80401-3393		10. SPONSORING/MONITORING AGENCY REPORT NUMBER  NREL/SR-520-34826		
11. SUPPLEMENTARY NOTES NREL Technical Monitor: Richard Matson				
12a. DISTRIBUTION/AVAILABILITY STATEMENT National Technical Information Service U.S. Department of Commerce 5285 Port Royal Road Springfield, VA 22161			12b. DISTRIBUTION CODE	
13. ABSTRACT ( <i>Maximum 200 words</i> ): Despite occasional experimental hints, medium-range structural order in covalently bonded amorphous semiconductors had largely escaped detection until the advent of fluctuation electron microscopy (FEM) in 1996. Using FEM, we find that every sample of amorphous silicon and germanium we have investigated, regardless of deposition method or hydrogen content, is rich in medium-range order. The paracrystalline structural model, which consists of small, topologically ordered grains in an amorphous matrix, is consistent with the FEM data; but due to strain effects, materials with a paracrystalline structure appear to be amorphous in diffraction measurements. We present measurements on hydrogenated amorphous silicon deposited by different methods, some of which are reported to have greater stability against the Staebler-Wronski effect. FEM reveals that the matrix material of these samples is relatively similar, but the order changes in different ways upon both light soaking and thermal annealing. Some materials are inhomogeneous, with either nanocrystalline inclusions or large area-to-area variation in the medium-range order. We cite recent calculations that electronic states in the conduction band tail are preferentially located around the boundaries of the nm-scale paracrystalline regions that we have identified. This is new evidence in support of spatially inhomogeneous conduction mechanisms in a-Si. The key discovery in our work is that <i>all</i> samples of amorphous silicon must be described as having nm-scale topological crystalline order. This strongly modifies the long-standing model of a covalent random network. Our new understanding of medium-range order must be considered in all future models of electronic properties and the Staebler-Wronski effect.				
14. SUBJECT TERMS: PV; medium-range order; amorphous silicon; fluctuation electron microscopy (FEM); Staebler-Wronski effect; paracrystalline; variable coherence microscopy; magnetron sputtering; photostructural;			15. NUMBER OF PAGES	
			16. PRICE CODE	
17. SECURITY CLASSIFICATION OF REPORT Unclassified	18. SECURITY CLASSIFICATION OF THIS PAGE Unclassified	19. SECURITY CLASSIFICATION OF ABSTRACT Unclassified	20. LIMITATION OF ABSTRACT  UL	